

# EVIDENCE FOR A MASSIVE, EXTENDED CIRCUMGALACTIC MEDIUM AROUND THE ANDROMEDA GALAXY<sup>1</sup>

NICOLAS LEHNER<sup>2</sup>, J. CHRISTOPHER HOWK<sup>2</sup>, AND BART P. WAKKER<sup>3</sup>

*Accepted by the ApJ*

## ABSTRACT

We demonstrate the presence of an extended and massive circumgalactic medium (CGM) around Messier 31 using archival *HST* COS ultraviolet spectroscopy of 18 QSOs projected within two virial radii of M31 ( $R_{\text{vir}} = 300$  kpc). We detect absorption from Si III at  $-300 \lesssim v_{\text{LSR}} \lesssim -150$  km s<sup>-1</sup> toward all 3 sightlines at  $R \lesssim 0.2R_{\text{vir}}$ , 3 of 4 sightlines at  $0.8 \lesssim R/R_{\text{vir}} \lesssim 1.1$ , and possibly 1 of 11 at  $1.1 < R/R_{\text{vir}} \lesssim 1.8$ . We present several arguments that the gas at these velocities observed in these directions originates from the CGM of M31 rather than the Local Group or Milky Way CGM or Magellanic Stream. We show that the dwarf galaxies located in the CGM of M31 have very similar velocities over similar projected distances from M31. We find a non-trivial relationship only at these velocities between the column densities ( $N$ ) of all the ions and  $R$ , whereby  $N$  decreases with increasing  $R$ . Singly ionized species are only detected in the inner CGM of M31 at  $< 0.2R_{\text{vir}}$ . At  $R < 0.8R_{\text{vir}}$ , the covering fraction is close to unity for Si III and C IV ( $f_c \sim 60\%–97\%$  at the 90% confidence level), but drops to  $f_c \lesssim 10\%–20\%$  at  $R \gtrsim R_{\text{vir}}$ . We show that the M31 CGM gas is bound, multiphase, predominantly ionized (i.e., H II  $\gg$  H I), and becomes more highly ionized gas at larger  $R$ . We estimate using Si II, Si III, and Si IV a CGM metal mass of at least  $2 \times 10^6 M_{\odot}$  and gas mass of  $\gtrsim 3 \times 10^9 (Z_{\odot}/Z) M_{\odot}$  within  $0.2R_{\text{vir}}$ , and possibly a factor  $\sim 10$  larger within  $R_{\text{vir}}$ , implying substantial metal and gas masses in the CGM of M31. Compared with galaxies in the COS-Halos survey, the CGM of M31 appears to be quite typical for a  $L^*$  galaxy.

*Keywords:* galaxies: halos — galaxies: individual (M31) — intergalactic medium — Local Group — quasars: absorption lines

## 1. INTRODUCTION

The circumgalactic medium (CGM), loosely defined as the diffuse gas between the thick disk of galaxies and about a virial radius of galaxies is the scene where large-scale inflow and outflow from galaxies takes place. The competition between these processes is thought to shape galaxies and drive their evolution (e.g., Kereš et al. 2005; Dekel & Birnboim 2006; Faucher-Giguère & Kereš 2011; Putman et al. 2012). Observations of the properties of the CGM are therefore critical to test theories of galaxy evolution. Recent discoveries using high quality ultraviolet observations show that the CGM is a pivotal component of galaxies with significant mass of baryons and metals (e.g., Wakker & Savage 2009; Chen et al. 2010; Prochaska et al. 2011; Tumlinson et al. 2011; Churchill et al. 2012; Kacprzak et al. 2012, 2014; Werk et al. 2013, 2014; Lehner et al. 2013; Stocke et al. 2013; Peeples et al. 2014; Werk et al. 2014; Liang & Chen 2014; Bordoloi et al. 2014).

Observations of the CGM at  $z > 0$  typically provide only average properties of the CGM along one sightline (in some rare cases, 2–3 sightlines, e.g., Keeney et al.

2013), and therefore the CGM properties such as gas kinematics, metal mass distribution, and ionization states as a function of galaxy geometry and properties are not well constrained. One way to alleviate in part this issue is to determine the properties of the CGM for similar type or mass of galaxies with sightlines piercing their CGM at various impact parameters. This is the strategy used in the COS-Halos survey (Tumlinson et al. 2013). With a controlled sample of  $L^*$  galaxies, the COS-Halos survey provided strong evidence for extended highly ionized CGM by demonstrating that typical star-forming  $L^*$  galaxies have O VI column densities  $N_{\text{OVI}} \gtrsim 10^{14.3}$  cm<sup>-2</sup>, while more passive  $L^*$  galaxies show weaker or no O VI absorption in their CGM (Tumlinson et al. 2011). While this experiment has been extremely fruitful (Thom et al. 2011, 2012; Tumlinson et al. 2011, 2013; Werk et al. 2013, 2014; Peeples et al. 2014), the COS-Halos galaxies have enough spread in their properties that even collectively they do not mimic a single galaxy.

With several tens of QSO sightlines going through the Milky Way (MW) CGM (e.g., Savage et al. 2003; Sembach et al. 2003; Wakker et al. 2003, 2012; Fox et al. 2006; Shull et al. 2009; Lehner et al. 2012), the MW would appear a perfect candidate for a “zoom-in” experiment, i.e., in which we can study the CGM along different sightlines of a single galaxy. However, our understanding of the MW CGM has remained somewhat limited by our position within the MW disk. The high-velocity clouds (HVCs, clouds that have typically  $|v_{\text{LSR}}| \geq 90$  km s<sup>-1</sup> at  $|b| \gtrsim 20^\circ$ , e.g., Wakker 2001) that cover the Galactic sky were thought to possibly probe the ex-

<sup>1</sup> Based on observations made with the NASA/ESA Hubble Space Telescope, obtained at the Space Telescope Science Institute, which is operated by the Association of Universities for Research in Astronomy, Inc. under NASA contract No. NAS5-26555.

<sup>2</sup> Department of Physics, University of Notre Dame, 225 Nieuwland Science Hall, Notre Dame, IN 46556

<sup>3</sup> Supported by NASA/NSF, affiliated with the Department of Astronomy, University of Wisconsin, 475 N. Charter Street, Madison, WI 53706

tended MW CGM. Their distances are now largely determined (Ryans et al. 1997; Wakker 2001; Thom et al. 2006, 2008; Wakker et al. 2007, 2008; Lehner & Howk 2010; Smoker et al. 2011 for H I HVC complexes and Lehner & Howk 2011; Lehner et al. 2012 for the diffuse ionized HVCs, iHVCs), but this created another puzzle since they place most of the H I HVCs and iHVCs within 5–15 kpc of the sun, not at 100–300 kpc, the expected size of the MW CGM, and hence the HVCs only represent a comparatively very small mass (since  $M \propto d^2$ ). Only the Magellanic Stream (MS, e.g., Putman et al. 1998; Brüns et al. 2005; Nidever et al. 2008; Fox et al. 2014) is more distant, possibly extending to 80–200 kpc (Besla et al. 2012), providing some indirect evidence for an extended corona around the MW (e.g., Stanimirović et al. 2002; Sembach et al. 2003; Fox et al. 2013, 2014).

The high O VI column density found by COS-Halos is another element that shows that the iHVCs do not probe the extended MW CGM since  $N_{\text{OVI}}$  for the MW iHVCs is on average a factor 5 times smaller (see the results in Sembach et al. 2003; Fox et al. 2006). Only if the entire MW thick disk and halo absorption is integrated, would  $N_{\text{OVI}}$  in the MW approach  $10^{14.3} \text{ cm}^{-2}$  (i.e., by combining the results of Savage et al. 2003 and Sembach et al. 2003). This would mean that most of the column density of the MW CGM might be hidden in part in the low-velocity gas often associated with the thin and thick disks (see Peek et al. 2009 and Y. Zheng et al. 2015, in preparation). However, it is also plausible that the MW CGM has properties that are different from  $z \sim 0.5 L^*$  galaxies.

Studies of the gas content of nearby galaxies offer major advantages over both the MW and higher redshift galaxies. Nearby galaxies span a large angular extent and can be studied over multiple lines-of-sight and offer a direct mapping between the stellar distribution and the gas content. This experiment has been conducted for the Large Magellanic Cloud (Howk et al. 2002; Lehner & Howk 2007; Lehner et al. 2009; Barger et al. 2014; N. Lehner et al., 2015 in prep.), showing in particular the presence of large-scale outflows from a sub- $L^*$  galaxy feeding in metals the CGM of a  $L^*$  galaxy (the MW).

The  $L^*$  galaxy that can be observed with the most detail is the Andromeda Nebula (M31). The stellar disk and halo of M31 have been subject to intense study (e.g., Brown et al. 2006; McConnachie et al. 2009; Gilbert et al. 2012, 2014; Dalcanton et al. 2012), with well-determined local and global properties, including its inclination (Walterbos & Kennicutt 1987), stellar and virial masses (Geehan et al. 2006; van der Marel et al. 2012), dust and ISM disk mass (Draine et al. 2014), rotation curve (e.g., Chemin et al. 2009), and its galaxy satellites (McConnachie 2012). These studies all imply that M31 is fairly typical of massive star-forming galaxies, which has undergone several major interactions with its satellites (e.g., Gordon et al. 2006; Putman et al. 2009), and possibly in a phase of transformation into a red galaxy (Mutch et al. 2011; Davidge et al. 2012). The specific star-formation rate of M31,  $\text{sSFR} \equiv \text{SFR}/M_\star = (5 \pm 1) \times 10^{-12} \text{ yr}^{-1}$  (using the stellar mass  $M_\star$  and SFR from Geehan et al. 2006; Kang et al. 2009), places

M31 just between the passively evolving and star forming galaxies in COS-Halos (Tumlinson et al. 2011). As we show in this paper, the value of  $N_{\text{OVI}}$  in the CGM of M31 and the sSFR of M31 are also consistent with M31 being in the “green valley”.

Parallel to this intensive observational effort, there is also a major theoretical effort to understand the two massive galaxies, the MW and M31, of the Local Group (LG) (Richter 2012; Garrison-Kimmel et al. 2014; Nuza et al. 2014). With this large amount of empirical results, M31 could become a benchmark for assessing the validity of the physics implemented in these simulations. This requires to have also knowledge of its extended diffuse ionized CGM. Both deep and shallower observations of the H I 21-cm emission have reported detections of H I clouds mostly within 50 kpc (Thilker et al. 2004; Westmeier et al. 2005, 2008), and at farther distances along the M31–M33 axis (Braun & Thilker 2004). The H I 21-cm emission 49' resolution map in Braun & Thilker (2004) gave the impression of an H I bridge between M31 and M33, but subsequent deep Green Bank Telescope (GBT) 9'1 resolution observations show that they appear to be small concentrations of H I with  $\sim 10^5 M_\odot$  on scale of a few kpc (Lockman et al. 2012; Wolfe et al. 2013). As for the MW, these H I clouds might only be the tip of the iceberg and H I alone does not provide information on the gas-phases, the metal content, and hence the total metal and baryon masses of the gas in the CGM of M31.

We therefore mined the *HST* Cosmic Origins Spectrograph (COS) archive for high resolution UV QSO spectra with sufficient signal-to-noise (S/N) to search and model the weak metal-line absorption features that may be signatures of the diffuse CGM gas of M31. Our search radius is within about 2 virial radii of M31. We adopt throughout a distance of 752 kpc and a virial radius of  $R_{\text{vir}} = 300$  kpc for M31 (Riess et al. 2012; van der Marel et al. 2012).<sup>4</sup> In §2, we describe in detail how the sample was selected, while in §3 we present several arguments that point to an association to the diffuse CGM of M31 for the absorption at  $-300 \lesssim v_{\text{LSR}} \lesssim -150 \text{ km s}^{-1}$  observed along some of the sightlines in our sample. In §4, we determine the properties of the M31 CGM, including its kinematics, ionization, covering fraction, and baryon and metal masses. We discuss the implications of our findings in §5 and finally summarize our results in §6.

## 2. SAMPLE AND DATA ANALYSIS

In the *HST* COS archive at the Mikulski Archive for Space Telescopes (MAST), we identify 31 targets at projected distances  $R < 2R_{\text{vir}}$  from M31 that were ob-

<sup>4</sup> We emphasize that the exact definition of CGM and even  $R_{\text{vir}}$  is far from settled, as recently discussed by Shull (2014). For example, the overdensity  $\Delta_{\text{vir}} = 18\pi^2 = 178 \approx 200$  of a collapsed object to estimate  $R_{\text{vir}}$  is often calculated assuming a “top-hat” model in an Einstein-de Sitter cosmology, but this value changes with the adopted cosmological models (e.g., Klypin et al. 2002 adopted  $\Delta_{\text{vir}} = 340$ ; see discussion in Shull 2014). For ease of comparison with previous studies and in view of the distribution of our targets we choose for this paper  $R_{\text{vir}} = 300$  kpc for Andromeda. As we show in this paper, the gas that we associate with the CGM of M31 is at velocities consistent with the material being gravitationally bound to M31 (even beyond  $R_{\text{vir}}$ ), which implies that the extended CGM gas of M31 is bound.

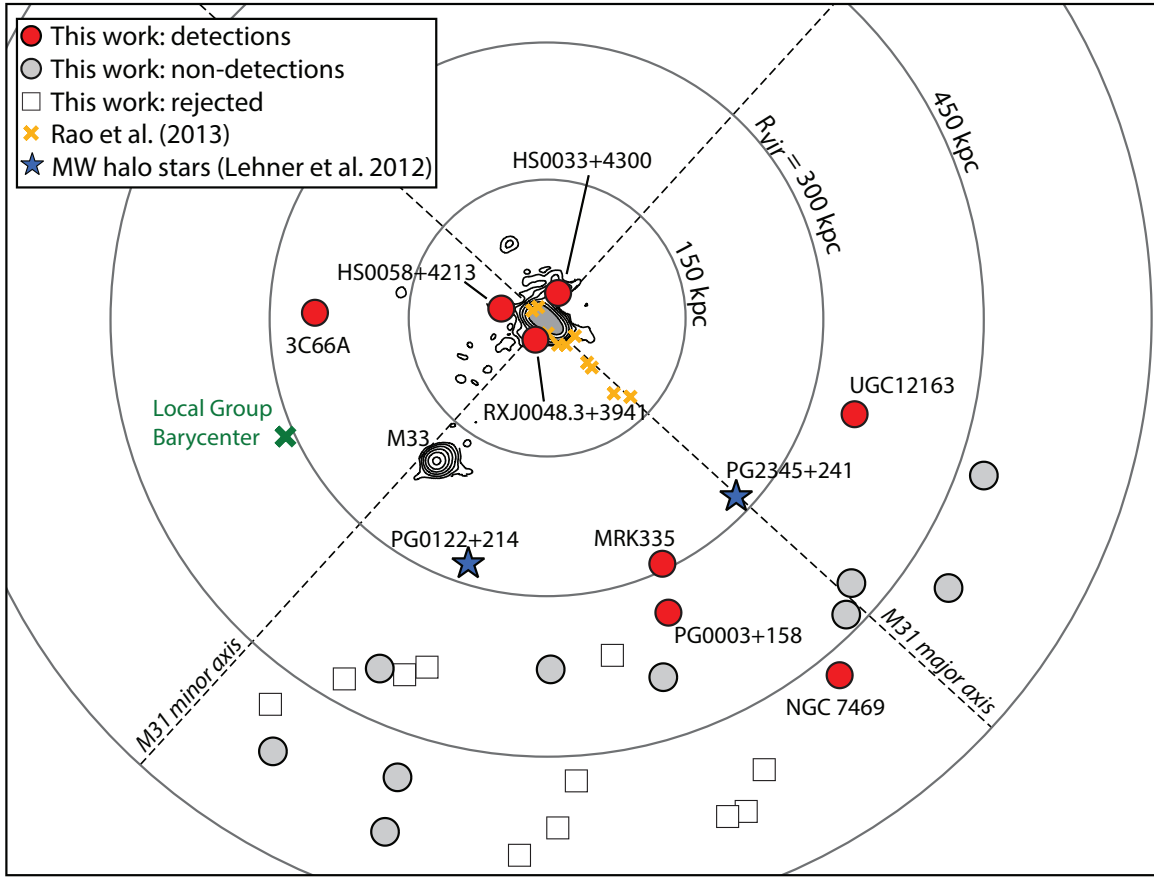


**Figure 1.** Distribution of our targets in our adopted (circles) and rejected (squares) samples used to probe the CGM of M31 (right ascension increases from right to left, declination increases from bottom to top, see Table 1). All these sightlines were observed with COS G130M and/or G160M and some were also observed with *FUSE*. Targets with UV absorption at LSR velocities  $-300 \leq v_{\text{LSR}} \leq -150$   $\text{km s}^{-1}$  associated with the CGM of M31 are shown in red. Note that the sightline HS0058+4213 is near the  $0.2R_{\text{vir}}$  boundary. Overplotted is the H I 21-cm emission map around M31 adapted from Braun & Thilker (2004) where the lowest contour has  $\log N_{\text{HI}} = 17.5$  in the  $40'$  beam, with 0.5 dex increment between contours (this provides in our opinion a better representation of the H I distribution around M31 according to recent GBT observations, see Lockman et al. 2012; Wolfe et al. 2013). The yellow crosses show for reference the targets from the COS G140L M31 program where low ions (e.g., Mg II) were detected only within the H I disk contour (i.e.,  $R \leq 32$  kpc, see Rao et al. 2013). The two MW stars in blue are distant halo stars, allowing us to determine that absorption at  $v_{\text{LSR}} \gtrsim -170$   $\text{km s}^{-1}$  traces MW gas. We also indicate the position of the Local Group barycenter with the green cross.

served with the COS G130M and/or G160M gratings ( $R_{\lambda} \approx 16,000$ ). In Table 1, we summarize the 18 sightlines that are included in the adopted sample and the 13 sightlines rejected for the main analysis of the M31 CGM absorption. The two chief reasons for excluding sightlines are either the signal-to-noise (S/N) level is too low ( $S/N \lesssim 4$ ) or there is a clear contamination from the MS or unrelated absorbers; the exact reasons for the exclusion of each sightline are given in the table footnotes

and in §3, where we discuss the absorption velocity structure toward M31. In Fig. 1, we show the distribution of the targets in our sample overplotted with the H I contours from Braun & Thilker (2004). The three inner targets are also part of another paper that will consider in more detail the relation (if any) between the gas and stellar halos of M31 (C. Danforth et al. 2015, in prep.); only these targets were initially from a program aimed to study specifically the halo of M31 (*HST* program 11632, PI: R. Rich).

**Table 1**  
Sample of COS G130M-G160M Targets Piercing the CGM of M31

Target	RA ( $^{\circ}$ )	DEC ( $^{\circ}$ )	$z_{\text{em}}$	$R$ (kpc)	COS	S/N	Note
Adopted Sample							
RXJ0048.3+3941	12.08	+39.69	0.134	25	G130M-G160M	23	1
HS0033+4300	9.096	+43.28	0.120	31	G130M-G160M	5	1
HS0058+4213	15.38	+42.49	0.190	49	G130M-G160M	6	1
3C66A	35.67	+43.04	0.340	239	G130M-G160M	16	1
MRK335	1.58	+20.20	0.034	287	G130M-G160M	20	1
PG0003+158	1.50	+16.16	0.450	334	G130M-G160M	16	1
UGC12163	340.66	+29.73	0.025	340	G130M-G160M	9	1

Table 1 — *Continued*

Target	RA (°)	DEC (°)	$z_{\text{em}}$	$R$ (kpc)	COS	S/N	Note
MRK1502	13.40	+12.69	0.061	361	G130M	7	1
MRK1501	2.63	+10.984	0.090	389	G130M	9	1
SDSSJ015952.95+134554.3	29.97	+13.77	0.504	401	G130M	7	1
3C454.3	343.49	+16.15	0.859	424	G130M–G160M	5	1
SDSSJ225738.20+134045.0	344.41	+13.68	0.594	440	G130M–G160M	6	1
NGC7469	345.82	+8.87	0.016	475	G130M–G160M	24	1
HS2154+2228	329.20	+22.713	1.290	476	G160M	7	1
PHL1226	28.62	+4.81	0.404	482	G130M	8	1
MRK304	334.30	+14.24	0.067	499	G130M–G160M	20	1
MRK595	40.40	+7.19	0.027	514	G130M	8	1
MRK1014	29.96	+0.40	0.164	527	G130M	22	1
Rejected Sample							
PG0026+129	7.31	+13.277	0.142	355	G130M	12	2
SDSSJ014143.20+134032.0	25.43	+13.685	0.045	381	G130M	3	3
IRAS01477+1254	27.62	+13.159	0.147	396	G130M–G160M	3	3
SDSSJ021348.53+125951.4	33.45	+13.007	0.228	427	G130M–G160M	2	3
PG0044+030	11.77	+3.331	0.624	462	G130M	6	4
4C10.08	40.62	+11.026	2.680	484	G130M	0	3
LBQS0052-0038	13.86	−0.363	0.167	501	G130M–G160M	4	3
NGC7714	354.06	+2.165	0.009	502	G130M–G160M	8	5
PG2349-014	357.98	−1.153	0.174	522	G130M	7	6
LBQS0107-0232	17.56	−2.282	0.728	522	G160M	9	7
LBQS0107-0233	17.57	−2.314	0.956	523	G130M–G160M	9	8
LBQS0107-0235	17.56	−2.331	0.960	523	G130M–G160M	9	8
SDSSJ234500.43-005936.0	356.25	−0.993	0.789	525	G130M–G160M	5	9

**Note.** — 1: All the targets in the adopted sample satisfied the following criteria: i)  $S/N \gtrsim 5$  in at least one transition, ii) there is no obvious contamination in the  $-300 \lesssim v_{\text{LSR}} \lesssim -150$   $\text{km s}^{-1}$  component from the MS in the direction of the target. 2: Weak absorption features are observed between  $-300$  and  $-180$   $\text{km s}^{-1}$  in the profiles of C II, Si II, Si III, and Si IV, but there is no match in the velocity centroids between all the observed transitions (including for the Si IV doublet), implying that there is some contamination from unrelated absorbers for several of the observed transitions. 3: These data have too low S/N. 4: Two absorption components at  $-290$  and  $-210$   $\text{km s}^{-1}$ , but at this RA, DEC, both are more likely to have a MS origin. 5: Smeared absorption lines owing to the extended background object. 6: This sightline pierces the MS and has a MS component centered at  $-300$   $\text{km s}^{-1}$  that extends from  $-400$  to  $-190$   $\text{km s}^{-1}$ . 7: Only C IV is available and both transitions of the doublet are contaminated. 8: Absorption is observed at  $-250$   $\text{km s}^{-1}$  in Si III and C IV, but at this RA, DEC, it is likely from the MS (this sightline is about  $20^\circ$  off the MS body). 9: This sightline pierces the MS and has a MS component centered at  $-250$   $\text{km s}^{-1}$  that extends from  $-350$  to  $-150$   $\text{km s}^{-1}$ .

We also searched the *Far Ultraviolet Spectroscopic Explorer* (*FUSE*,  $R_\lambda \approx 15,000$ ) archive to complement the COS data with the O VI absorption. The following targets have *FUSE* observations with adequate S/N (i.e.,  $\gtrsim 5$ ): RXJ0048.3+3941, MRK335, UGC12163, and NGC7469. We, however, do not consider *FUSE* data with no COS observation because the available UV transitions in the far-UV spectrum (O VI, C II, C III, Si II) are either too weak or too contaminated to allow us to reliably identify individual velocity components in their absorption profiles.

Information on the design and performance of COS and *FUSE* can be found in Green et al. (2012) and Moos et al. (2000), respectively. Detailed information about the COS and *FUSE* data processing can be found in Fox et al. (2014) and Wakker et al. (2003). In short, the exposures are aligned in wavelength space by matching the centroids of all the absorption lines visible in

individual spectra. The coadded spectrum for each object is then shifted into the local standard of rest (LSR) velocity frame by matching the centroids of the Galactic H I 21-cm emission in that direction from the LAB survey (Kalberla et al. 2005) to the absorption of neutral and singly ionized species. We normalize the QSO continua with low order Legendre polynomials within about  $\pm 1000$   $\text{km s}^{-1}$  from the absorption under consideration; typically polynomials with orders  $m \leq 4$  are fitted. In Fig. 2, we show an example of the normalized profiles of selected ions for RXJ0048.1+3941. In the figures of the Appendix, we show all the normalized profiles of our selected targets against the LSR velocity. The O VI can be contaminated by  $\text{H}_2$  absorption, and we remove this contamination following the method described in Wakker (2006). We show the  $\text{H}_2$  model in the figures of the Appendix. Based on previous experience, this contamination can be removed fairly accurately with an uncertainty of about  $\pm 0.1$  dex on the column density (Wakker et al. 2003).

To search for M31 CGM absorption and to determine the properties of the CGM gas, we consider the following atomic and ionic transitions: O I  $\lambda 1302$ , C II  $\lambda 1334$ , C III  $\lambda 977$ , C IV  $\lambda \lambda 1548, 1550$ , Si II  $\lambda 1193$  (Si II  $\lambda 1260$  is blended with S II  $\lambda 1259$  near the systemic velocity of M31), Si III  $\lambda 1206$ , Si IV  $\lambda \lambda 1393, 1402$ , as well as O VI  $\lambda \lambda 1031, 1037$  for the four sightlines observed with *FUSE*. Other transitions are typically too weak to be detected and do not produce interesting limits.

We use the apparent optical depth (AOD) method described by Savage & Sembach (1991) to estimate the total column density and average velocity of the metal ions. The absorption profiles are converted into apparent column densities per unit velocity,  $N_a(v) = 3.768 \times 10^{14} \ln[F_c(v)/F_{\text{obs}}(v)] / (f\lambda) \text{ cm}^{-2} (\text{km s}^{-1})^{-1}$ , where  $F_c(v)$  and  $F_{\text{obs}}(v)$  are the modeled continuum and observed fluxes as a function of velocity, respec-

tively,  $f$  is the oscillator strength of the transition and  $\lambda$  is the wavelength in Å. The atomic parameters are for the UV transitions from Morton (2003). When no detection was observed, we estimated a  $3\sigma$  upper limit following the method described by Lehner et al. (2008). The total column density was obtained by integrating over the absorption profile  $N = \int_{v_1}^{v_2} N_a(v)dv$  and the average velocity was determined from the first moment  $\langle v \rangle = \int_{v_1}^{v_2} v N_a(v)dv / \int_{v_1}^{v_2} N_a(v)dv$ .

We consider absorption over the velocities that we associate with the CGM of M31 (see the component in red in Fig. 2); see §3 for several arguments that support this association. In Table 2, we summarize the integration range for each sightline and the velocity and column density results for each species. We find a good agreement between the column densities estimated for the doublet transitions (C IV, Si IV), showing no indication of saturation or contamination. We note, however, that C II and Si III for the 3 targets at  $R \leq 50$  kpc ( $R \leq 0.2R_{\text{vir}}$ ) could be somewhat saturated owing the peak apparent optical depth being  $\tau_a \gtrsim 1$ . In this table, we also list the average velocity (defined as  $\langle v_{\text{all}} \rangle$ ) based on all the reliable transitions for a given sightline. For the sightlines where no M31 absorption is found, we derive a  $3\sigma$  upper limit using generally the velocity interval  $[-280, -150]$  km s $^{-1}$  to mimic the velocity range of the absorption attributed to the M31 CGM observed within  $0.2R_{\text{vir}}$ .

**Table 2**  
Kinematics and Column Densities

Species	$(v_1, v_2)$ (km s $^{-1}$ )	$\langle v \rangle$ (km s $^{-1}$ )	$\log N$ [cm $^{-2}$ ]
RXJ0048.3+3941, $R = 25$ kpc, $\langle v_{\text{all}} \rangle = -213.1 \pm 8.7$ km s $^{-1}$			
O I $\lambda 1302$	-306, -150	...	< 13.63
C II $\lambda 1334$	-306, -150	-188.7 :	14.57 :
Si II $\lambda 1193$	-306, -150	-197.4 $\pm$ 2.0	13.43 $\pm$ 0.02
C III $\lambda 977$	-306, -150	-220.7 :	> 14.08
Si III $\lambda 1206$	-306, -150	-215.5 $\pm$ 0.8	13.42 $\pm$ 0.01
Si IV $\lambda 1393$	-306, -150	-212.9 $\pm$ 1.3	13.38 $\pm$ 0.01
Si IV $\lambda 1402$	-306, -150	-211.3 $\pm$ 2.6	13.41 $\pm$ 0.03
C IV $\lambda 1548$	-306, -150	-218.8 $\pm$ 1.1	14.08 $\pm$ 0.02
C IV $\lambda 1550$	-306, -150	-222.7 $\pm$ 2.0	14.11 $\pm$ 0.02
O VI $\lambda 1031$	-306, -130	-209.4 $\pm$ 5.0	14.38 $\pm$ 0.12
HS0033+4300, $R = 31$ kpc, $\langle v_{\text{all}} \rangle = -204.1 \pm 2.0$ km s $^{-1}$			
O I $\lambda 1302$	-280, -150	...	< 14.26
C II $\lambda 1334$	-280, -150	-204.1 $\pm$ 5.9	14.34 :
Si II $\lambda 1193$	-280, -150	-223.8 :	13.36 $\pm$ 0.18
Si III $\lambda 1206$	-280, -150	-201.2 $\pm$ 6.4	13.31 $\pm$ 0.10
Si IV $\lambda 1402$	-280, -150	-206.8 $\pm$ 6.7	13.26 $\pm$ 0.09
C IV $\lambda 1548$	-280, -150	-203.6 $\pm$ 3.0	14.04 $\pm$ 0.05
C IV $\lambda 1550$	-280, -150	-204.6 $\pm$ 5.5	14.07 $\pm$ 0.08
HS0058+4213, $R = 48$ kpc, $\langle v_{\text{all}} \rangle = -211.1 \pm 3.9$ km s $^{-1}$			
O I $\lambda 1302$	-280, -150	...	< 14.02
C II $\lambda 1334$	-280, -150	-214.1 $\pm$ 2.9	14.41 $\pm$ 0.06
Si II $\lambda 1193$	-280, -150	-217.3 $\pm$ 5.9	13.45 $\pm$ 0.08
Si III $\lambda 1206$	-280, -150	-210.5 $\pm$ 3.2	13.44 $\pm$ 0.08
Si IV $\lambda 1393$	-280, -150	-207.4 $\pm$ 5.1	13.42 $\pm$ 0.07
Si IV $\lambda 1402$	-280, -150	-212.4 $\pm$ 8.7	13.43 $\pm$ 0.12
C IV $\lambda 1548$	-280, -150	-210.5 $\pm$ 4.3	13.95 $\pm$ 0.06
C IV $\lambda 1550$	-280, -150	-205.8 $\pm$ 7.6	14.00 $\pm$ 0.10
3C66A, $R = 239$ kpc, $\langle v_{\text{all}} \rangle = -256.0 \pm 4.9$ km s $^{-1}$			
O I $\lambda 1302$	-321, -214	...	< 13.54
C II $\lambda 1334$	-321, -214	...	< 13.10

**Table 2** — *Continued*

Species	$(v_1, v_2)$ (km s $^{-1}$ )	$\langle v \rangle$ (km s $^{-1}$ )	$\log N$ [cm $^{-2}$ ]
Si II $\lambda 1193$	-321, -214	...	< 12.54
Si III $\lambda 1206$	-321, -214	-256.0 $\pm$ 4.9	$\leq$ 12.48 $\pm$ 0.07
Si IV $\lambda 1393$	-321, -214	...	< 13.04
C IV $\lambda 1548$	-321, -214	...	< 13.02
MRK335, $R = 287$ kpc, $\langle v_{\text{all}} \rangle = -240.1 \pm 5.2$ km s $^{-1}$			
O I $\lambda 1302$	-275, -180	...	< 13.43
C II $\lambda 1334$	-275, -180	...	< 12.98
C III $\lambda 977$	-275, -180	-222.4 :	> 14.09
Si II $\lambda 1193$	-275, -180	...	< 12.42
Si III $\lambda 1206$	-275, -150	-238.5 $\pm$ 5.6	12.41 $\pm$ 0.06
Si IV $\lambda 1393$	-275, -180	-241.1 $\pm$ 6.3	12.62 $\pm$ 0.09
Si IV $\lambda 1402$	-275, -150	-247.9 $\pm$ 15.5	12.69 $\pm$ 0.15
C IV $\lambda 1548$	-275, -180	-233.7 $\pm$ 2.5	13.48 $\pm$ 0.04
C IV $\lambda 1550$	-275, -180	-239.1 $\pm$ 5.6	13.40 $\pm$ 0.10
O VI $\lambda 1031$	-275, -180	-222.0 $\pm$ 1.0	14.10 $\pm$ 0.13
PG0003+158, $R = 334$ kpc, $\langle v_{\text{all}} \rangle = -232.8 \pm 4.4$ km s $^{-1}$			
O I $\lambda 1302$	-275, -186	...	< 13.59
Si II $\lambda 1193$	-275, -186	...	< 12.48
Si III $\lambda 1206$	-275, -186	-235.6 $\pm$ 2.4	12.63 $\pm$ 0.04
Si IV $\lambda 1393$	-275, -186	-226.5 $\pm$ 7.2	12.51 $\pm$ 0.13
C IV $\lambda 1548$	-275, -186	-235.8 $\pm$ 2.9	13.28 $\pm$ 0.06
C IV $\lambda 1550$	-275, -186	-233.4 $\pm$ 6.6	13.22 $\pm$ 0.16
UGC12163, $R = 339$ kpc, $\langle v_{\text{all}} \rangle = -274.3 \pm 5.1$ km s $^{-1}$			
O I $\lambda 1302$	-280, -150	...	< 14.08
C II $\lambda 1334$	-280, -150	...	< 13.53
Si II $\lambda 1193$	-280, -150	...	< 13.00
Si III $\lambda 1206$	-280, -150	...	< 12.54
Si IV $\lambda 1393$	-280, -150	...	< 12.95
C IV $\lambda 1548$	-280, -150	...	< 13.35
O VI $\lambda 1031$	-320, -200	-274.3 $\pm$ 5.1	$\leq$ 14.20 $\pm$ 0.17
MRK1502, $R = 361$ kpc			
C II $\lambda 1334$	-280, -150	...	< 13.48
Si II $\lambda 1193$	-280, -150	...	< 12.85
Si III $\lambda 1206$	-280, -150	...	< 12.57
Si IV $\lambda 1393$	-280, -150	...	< 12.97
MRK1501, $R = 389$ kpc			
C II $\lambda 1334$	-280, -150	...	< 13.33
SDSSJ015952.95+134554.3, $R = 401$ kpc			
C II $\lambda 1334$	-280, -150	...	< 13.56
Si II $\lambda 1193$	-280, -150	...	< 12.96
Si III $\lambda 1206$	-270, -220	...	< 12.29
Si IV $\lambda 1393$	-280, -150	...	< 12.93
3C454.3, $R = 424$ kpc			
C II $\lambda 1334$	-280, -150	...	< 13.70
Si II $\lambda 1193$	-280, -150	...	< 13.19
Si III $\lambda 1206$	-280, -150	...	< 12.79
Si IV $\lambda 1393$	-280, -150	...	< 13.07
C IV $\lambda 1548$	-280, -150	...	< 13.29
SDSSJ225738.20+134045.0, $R = 440$ kpc			
C II $\lambda 1334$	-280, -150	...	< 13.64
Si II $\lambda 1193$	-280, -150	...	< 13.14
Si III $\lambda 1206$	-280, -150	...	< 12.66
Si IV $\lambda 1393$	-280, -150	...	< 13.06
C IV $\lambda 1550$	-280, -150	...	< 13.71
NGC7469, $R = 475$ kpc, $\langle v_{\text{all}} \rangle = -239.4 \pm 3.3$ km s $^{-1}$			
O I $\lambda 1302$	-260, -205	...	< 13.28
C II $\lambda 1334$	-260, -205	-239.3 $\pm$ 2.6	13.16 $\pm$ 0.07
Si II $\lambda 1193$	-260, -205	...	< 12.23
Si III $\lambda 1206$	-260, -205	-241.9 $\pm$ 1.0	12.60 $\pm$ 0.03
Si IV $\lambda 1393$	-260, -205	-234.6 $\pm$ 1.7	12.74 $\pm$ 0.05
Si IV $\lambda 1402$	-260, -205	-243.6 $\pm$ 4.0	12.69 $\pm$ 0.10

Table 2 — *Continued*

Species	$(v_1, v_2)$ (km s <sup>-1</sup> )	$\langle v \rangle$ (km s <sup>-1</sup> )	$\log N$ [cm <sup>-2</sup> ]
C IV $\lambda 1548$	-260, -205	-237.0 $\pm$ 1.9	13.20 $\pm$ 0.05
C IV $\lambda 1550$	-260, -205	-240.0 $\pm$ 2.8	13.27 $\pm$ 0.08
O VI $\lambda 1031$	-260, -205	-230.3 $\pm$ 2.4	13.87 $\pm$ 0.15
HS2154+2228, $R = 476$ kpc			
C IV $\lambda 1550$	-270, -150	...	< 13.31
PHL1226, $R = 482$ kpc			
C II $\lambda 1334$	-280, -150	...	< 13.51
Si II $\lambda 1193$	-280, -150	...	< 12.92
Si III $\lambda 1206$	-280, -150	...	< 12.46
Si IV $\lambda 1402$	-280, -150	...	< 13.14
MRK304, $R = 495$ kpc			
C II $\lambda 1334$	-280, -150	...	< 13.02
Si II $\lambda 1193$	-280, -150	...	< 12.57
Si III $\lambda 1206$	-280, -150	...	< 12.14
Si IV $\lambda 1393$	-280, -150	...	< 12.47
C IV $\lambda 1548$	-280, -150	...	< 13.03
MRK595, $R = 514$ kpc			
C II $\lambda 1334$	-310, -180	...	< 13.47
Si II $\lambda 1193$	-310, -180	...	< 12.95
Si III $\lambda 1206$	-310, -180	...	< 12.51
Si IV $\lambda 1393$	-310, -180	...	< 12.86
MRK1014, $R = 527$ kpc			
C II $\lambda 1334$	-280, -150	...	< 13.33
Si II $\lambda 1193$	-280, -150	...	< 12.63
Si III $\lambda 1206$	-280, -150	...	< 12.18
Si IV $\lambda 1402$	-280, -150	...	< 12.84

**Note.** — All the velocities are in the LSR frame. The velocities  $v_1$  and  $v_2$  are the velocities used for the integration of the AOD profiles. A colon means that the estimate value is uncertain owing to blending. A “<” indicates that no absorption is detected and a  $3\sigma$  upper limit is reported. A “>” sign is lower limit because the absorption reaches the zero-flux level. A “ $\leq$ ” sign indicates that only one transition of one ion is detected; this sign emphasizes that the line could be contaminated. For the O VI, the errors are dominated by systematics from the correction of the H<sub>2</sub> contamination. When more than one transition is detected,  $\langle v_{\text{all}} \rangle$  is the average velocity between all the ions (observed with COS) where the detection is not blended or uncertain.

### 3. ABSORPTION VELOCITY STRUCTURE AND ASSOCIATION WITH M31

In the general direction of M31, the absorption seen in the QSO spectra is complex, with absorption possibly arising from the MW thick disk and halo, MS, M31 CGM, Local Group (LG), or unrelated absorbers at higher redshifts,  $z$ . Unrelated absorbers are ruled out because for all but two sightlines we use several species and different transitions of the same species to identify higher redshift absorbers. In Fig. 2, we show an example of the normalized profiles of C II, Si II, Si III and C IV for RXJ0048.1+3941 at a projected distance  $R = 25$  kpc from M 31 (see the normalized spectra in the Appendix for the entire sample). This sightline shows absorption in several complexes stretching from  $-490$  km s<sup>-1</sup> to  $+90$  km s<sup>-1</sup>. As we show below the absorption at  $v_{\text{LSR}} \gtrsim -150$  km s<sup>-1</sup> is associated with the MW disk and halo; when detected, the absorption at  $-430 \lesssim v_{\text{LSR}} \lesssim -300$  km s<sup>-1</sup> is mostly associated with the MS, while we associate the  $-300 \lesssim v_{\text{LSR}} \lesssim -150$

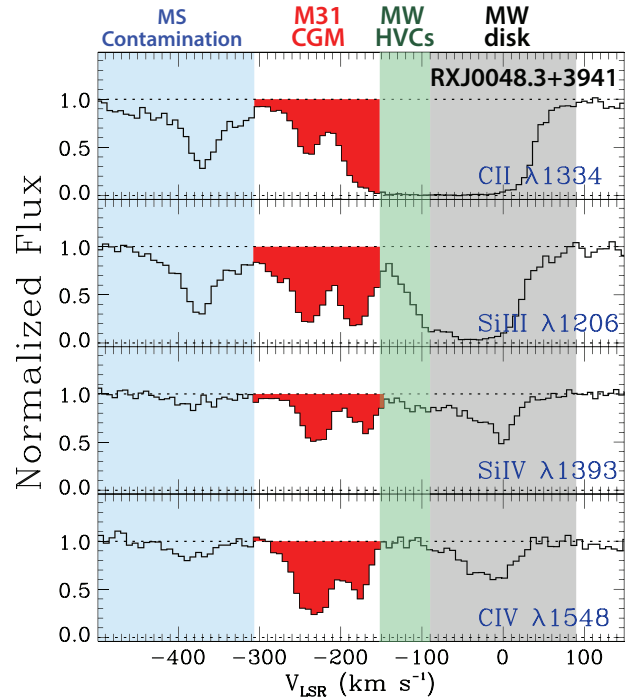


**Figure 2.** Normalized profiles of RXJ0048.1+3941 ( $R = 25$  kpc) as a function of the LSR velocity, where we highlight the origin of each component, the MS, the CGM of M31, and the MW disk and HVCS based on the arguments presented in §3. All the species for each selected sightline studied in this work are shown in the Appendix.

km s<sup>-1</sup> component with the CGM of M31.

#### 3.1. MW: absorption at $v_{\text{LSR}} \gtrsim -150$ km s<sup>-1</sup>

Both the MW thick disk and halo absorption can be readily identified in the direction of M31. Toward all the sightlines, saturated absorption is observed in C II, Si II, and Si III between about  $-90$  and  $+50$  km s<sup>-1</sup>. This absorption arises principally from the MW thick disk based on the Galactic disk rotation curve (Clemens 1985) and countless studies of the MW in UV absorption (e.g., Shull et al. 2009; Lehner et al. 2012; Wakker et al. 2012).

Toward many sightlines in our sample, absorption is also observed at velocities between about  $-170$  and  $-90$  km s<sup>-1</sup>. This absorption is from the MW iHVCs that are at distances of  $d \lesssim 10$ – $15$  kpc from the sun. We come to this conclusion for two reasons. First Lehner & Howk (2011) and Lehner et al. (2012) statistically constrained the distance of the iHVC population, showing that absorption at  $90 \leq |v_{\text{LSR}}| \lesssim 170$  km s<sup>-1</sup> is found typically in the lower halo of the MW, as it is observed at about the same rate toward MW halo stars and extragalactic AGN. Thus the gas seen in absorption toward M31 at  $-170 \lesssim v_{\text{LSR}} \lesssim -90$  km s<sup>-1</sup> corresponds to MW gas within 5–15 kpc of the sun. Second we show in Fig. 1 the locations of two MW halo stars near on the sky to M31 and M33 that were observed with COS (*HST* programs 12982 and 11592; PI: Lehner). These two stars are PG0122+214 ( $d = 9.6$  kpc), where HVC absorption is observed at  $v_{\text{LSR}} \simeq -160$  km s<sup>-1</sup> (see Lehner et al. 2012), and PG2345+241 ( $d = 4.9$  kpc, near the MRK335



sightline; see Fig. 1), where HVC absorption is seen at  $v_{\text{LSR}} \simeq -120 \text{ km s}^{-1}$ . In both cases, the HVC absorption is very weak and detected only in Si II and C II, not in C IV or Si IV, which are typically observed at  $-300 \lesssim v_{\text{LSR}} \lesssim -150 \text{ km s}^{-1}$  (Si III cannot be used in stellar spectra owing to the strong damping wings of  $\text{Ly}\alpha$ ). Thus gas at  $-150 \lesssim v_{\text{LSR}} \lesssim -90 \text{ km s}^{-1}$  is relatively close to the sun in this direction, and we therefore assign any absorption in our sample with velocity components centered on  $v_{\text{LSR}} \gtrsim -150 \text{ km s}^{-1}$  to the MW disk and its halo.

### 3.2. Identifying M31 CGM Gas

Several of our sightlines show absorption at  $v_{\text{LSR}} \lesssim -170 \text{ km s}^{-1}$ . Gas at these velocities has not been seen toward halo stars at  $d \lesssim 20 \text{ kpc}$  from the sun (see §3.1). We identify the absorption at  $-300 \lesssim v_{\text{LSR}} \lesssim -150 \text{ km s}^{-1}$  with the CGM of M31 for the following reasons:

1. These velocities differ by more than  $200 \text{ km s}^{-1}$  for some of the targets from the expected velocities of the MS in this direction (§3.2.1).
2. These velocities are similar to the velocities of the M31 dwarf satellites (§3.2.1).
3. There is a non-trivial relationship between the column densities of this component and the projected distances from M31 that only exists for gas in this velocity range (§3.2.2).
4. The detection rate of this component is high within a projected distance of  $300 \text{ kpc}$  (the virial radius) from M31 and plummets beyond  $300 \text{ kpc}$ , another property only observed for this velocity component (§3.2.2).
5. The H I emission observations have detected clouds in the M31 CGM at similar LSR velocities at projected distances  $\lesssim 100 \text{ kpc}$  (§3.2.3).

Each of these independent reasons alone points toward a M31 CGM origin. Combining all these observed properties of the absorption at  $-300 \lesssim v_{\text{LSR}} \lesssim -150 \text{ km s}^{-1}$  allows us to associate with very little doubt this population of clouds with the CGM of M31.

#### 3.2.1. Velocities

The MS extends over this part of the sky. In order to understand its potential signature in our observations, it is useful to plot the LSR velocity as a function of the MS longitude,  $l_{\text{MS}}$  (see Nidever et al. 2008 for the definition of the Magellanic Stream coordinate) since Nidever et al. (2008) found a tight relationship between the LSR velocity of the MS seen in H I emission and  $l_{\text{MS}}$ . In Fig. 3, the dashed line represents the average H I LSR velocity of the MS with  $l_{\text{MS}}$  determined from Fig. 9 of Nidever et al. (2008), which has a very small scatter in the velocity ( $\sim 20\text{--}30 \text{ km s}^{-1}$ ) at these  $l_{\text{MS}}$ ; there is no detection in H I emission (with the LAB sensitivity) beyond  $l_{\text{MS}} \lesssim -100^\circ$ . In each spectrum, we estimate the average velocities of the individual components in

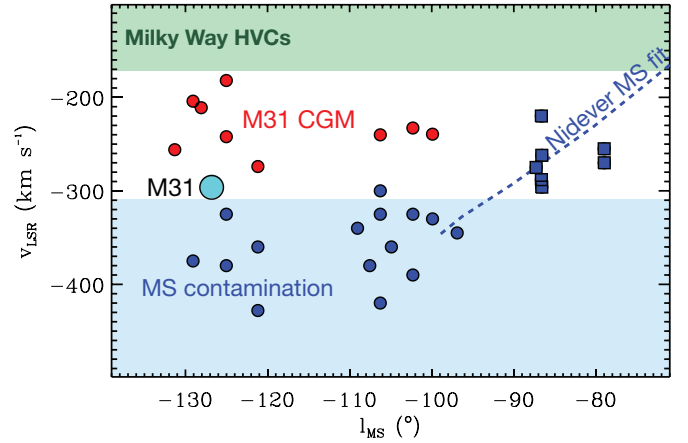


**Figure 3.** LSR velocity of the individual components centered at  $v_{\text{LSR}} < -170 \text{ km s}^{-1}$  identified in the spectra of the targets summarized in Table 1. The red and blue circles are from the adopted sample, while the blue squares are from the rejected sample. The cyan circle represents the systemic velocity of M31 at the M31 location. The dashed line represents the average velocities LSR velocities of H I estimated from the results by Nidever et al. (2008).

the velocity ranges  $-450 \lesssim v_{\text{LSR}} \lesssim -300 \text{ km s}^{-1}$  and  $-300 \lesssim v_{\text{LSR}} \lesssim -150 \text{ km s}^{-1}$ , which are represented by the blue and red circles in Fig. 3. We also show in this figure with blue squares the data from the rejected sample sightlines for individual components at  $v_{\text{LSR}} \lesssim -170 \text{ km s}^{-1}$ .

The blue squares are all at  $l_{\text{MS}} \geq -90^\circ$  where the MS is still observed in H I emission and where the expected MS are in the velocity range at  $-300 \lesssim v_{\text{LSR}} \lesssim -200 \text{ km s}^{-1}$ . That apparent association with the MS at  $-300 \lesssim v_{\text{LSR}} \lesssim -200 \text{ km s}^{-1}$  led us to reject them from the sample, so it is not surprising that the blue squares lie quite close to the dashed line. At  $-110^\circ \leq l_{\text{MS}} \leq -95^\circ$ , the blue circles are scattered around the general continuation of the dashed line. These mostly likely trace gas from the MS that extends beyond the dense H I body of the MS.

The  $-130^\circ \leq l_{\text{MS}} \leq -110^\circ$  longitudes are more than  $30^\circ\text{--}40^\circ$  from the MS seen in H I 21-cm emission. However, Sembach et al. (2003) and Fox et al. (2014) found UV absorption at the expected MS velocities extending  $30^\circ$  from the body of the MS tip seen in H I emission and concluded that this gas represents a diffuse extension of the MS seen only in metal line absorption. Braun & Thilker (2004) also noted extended H I emission filaments at the level  $\log N_{\text{HI}} > 17.3$  (i.e., a factor of 10 or more deeper than previous H I surveys) for velocities  $-430 \lesssim v_{\text{LSR}} \lesssim -330 \text{ km s}^{-1}$  that align with the expected extension of the MS (see their Figs. 3 and 5).<sup>5</sup> Based on these studies, it is likely that the blue circles in Fig. 3 at  $-130^\circ \leq l_{\text{MS}} \leq -120^\circ$  trace predominantly the

<sup>5</sup> The apparent smooth structures seen in Fig. 3 of Braun & Thilker (2004) are, however, questionable based on follow-up higher angular resolution GBT observations that reveal at least for the gas between M31 and M33 that the H I emission is typically resolved into cloud-like structure the size of a GBT beamwidth or smaller rather than elongated filamentary structure, and at much higher column densities (Lockman et al. 2012; Wolfe et al. 2013).

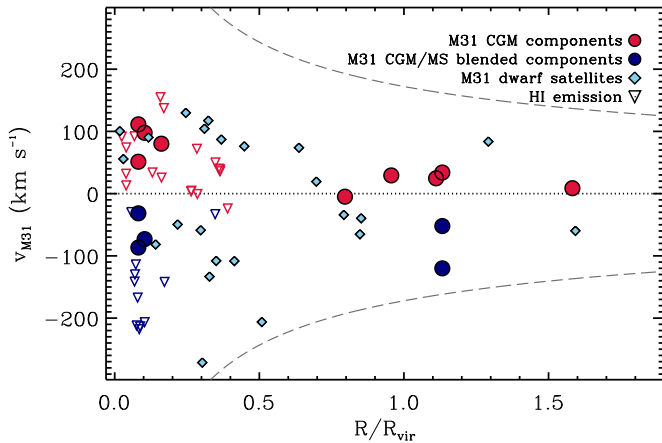


**Figure 4.** Comparison of the M31-centric velocities of the gas components seen in UV absorption and H I emission associated with the M31 CGM and the M31 galaxy satellites as a function of the projected distances from M31. For the blue circles, we only consider the data at  $l_{\text{MS}} < -120^\circ$ . The color coding for the circles is the same as those in Fig. 3. The color coding of the upside down triangles follows that of the circles. The dashed curves show the escape velocity for a  $10^{12} M_\odot$  point mass. The H I emission data are at  $R < 0.2R_{\text{vir}}$  from Westmeier et al. (2008) and at  $R \geq 0.2R_{\text{vir}}$  from Lockman et al. (2012) and Wolfe et al. (2013). The data for the galaxies associated with M31 were estimated from the parameters derived by McConnachie (2012).

MS, extending the tip of the MS observed in H I emission by more than  $30^\circ$ . If they are part of the MS, the velocity of the MS appears to flatten between  $l_{\text{MS}} \sim -130^\circ$  and  $-100^\circ$ . All the blue components at  $l_{\text{MS}} \gtrsim -110^\circ$  in Fig. 3 are within  $\lesssim 50 \text{ km s}^{-1}$  of the expected MS velocities.

On the other hand, the red circles at  $-130^\circ \leq l_{\text{MS}} \leq -120^\circ$  are at velocities incompatible with a MS origin by more than  $100\text{--}200 \text{ km s}^{-1}$ . At  $-110^\circ \leq l_{\text{MS}} \leq -95^\circ$ , they are about  $100 \text{ km s}^{-1}$  from the expected MS velocities determined by the dashed line, but only  $50 \text{ km s}^{-1}$  from some of the components marked as blue circles. Given their proximity to MS velocities, the origin of the component  $v_{\text{LSR}} \sim -220 \text{ km s}^{-1}$  toward MRK335, PG0003+158, and NGC7469 could potentially arise in the Stream. The first 2 sightlines have a MS latitude  $\sim 12^\circ$ , while NGC7469 has  $b_{\text{MS}} \simeq -5^\circ$ , i.e., NGC7469 goes through some of the H I emission from the MS (see Fig. 8 in Nidever et al. 2008), making NGC7469 the most uncertain sightline. NGC7469 is also the farther sightline from M31 with  $R \simeq 1.6R_{\text{vir}}$ . The other two sightlines lie at projected distances from M31  $R \approx R_{\text{vir}}$ .

From Fig. 3, it is also noticeable how the red and blue circles together appear quasi-symmetrically distributed around the systemic velocity of M31 at  $l_{\text{MS}} \lesssim -120^\circ$ . The component at negative velocities relative to M31 is, however, not observed in all the inner region sightlines, only toward RXJ0048.1+3941 ( $R = 25 \text{ kpc}$ ) and HS0033+4300 ( $R = 31 \text{ kpc}$ ) at  $v_{\text{LSR}} \simeq -380 \text{ km s}^{-1}$  and farther away toward UGC12163 ( $R = 339 \text{ kpc}$ ) at  $v_{\text{LSR}} \simeq -430 \text{ km s}^{-1}$  (strong absorption, see figure in Appendix), and  $-360 \text{ km s}^{-1}$  (weak absorption). The MS most certainly dominates the absorption of these components because 1) the properties of the absorption are reminiscent of those observed toward sightlines known to

probe the MS with strong absorption in C II and Si II as well as absorption in Si III, Si IV, and C IV (see, e.g., Fox et al. 2014), and 2) there is no difference in the strength of the absorption at projected distances from M31 of 25–31 kpc and 339 kpc (see §3.2.2). However, it is plausible that there is some absorption at these velocities from the M31 CGM gas that is strongly contaminated by the Magellanic Stream.

In order to learn more about the observed velocity distribution and determine if there is any similarity, we consider the dwarf galaxies that are located within the CGM of M31. McConnachie (2012) recently summarized the properties of the Local group galaxies, finding 23 of them associated with M31. For this comparison, it is useful to consider a “M31-centric” velocity defined as  $v_{\text{M31}} = v_{\text{GSR}}(\text{Obj}) - v_{\text{GSR}}(\text{M31}) \cos(\theta)$ , where  $v_{\text{GSR}} = v_{\text{LSR}} + 220 \sin(l) \cos(b)$  is the velocity of in the Galactic standard-of-rest (GSR) frame and  $\theta$  the angular separation of the galaxy or QSOs from M31. These velocities are very similar to the  $v_{\text{M31}}$  values listed in Table 2 of McConnachie (2012). Using the positions and radial velocities listed in Table 2 of his paper, we calculate the projected distances from M31 following the same method used for our sample and  $v_{\text{M31}}$  for each gas cloud in our sample and for each dwarf galaxy in the McConnachie (2012) sample. We use the projected distances since we do not know the distance of the absorbers in our sample from the M31. However, we stress the membership of each dwarf galaxies with M31 is based on distances from the sun that are between 525 kpc and 920 kpc and within  $< 2R_{\text{vir}}$  from M31 (see for more detail McConnachie 2012).

In Fig. 4, the distribution of  $v_{\text{M31}}$  as a function of  $R/R_{\text{vir}}$  is shown for the dwarf satellites and the gas seen in absorption at  $-300 \lesssim v_{\text{LSR}} \lesssim -150 \text{ km s}^{-1}$  (red circles) and  $-420 \lesssim v_{\text{LSR}} \lesssim -300 \text{ km s}^{-1}$  with  $-130^\circ \leq l_{\text{MS}} \leq -120^\circ$  (blue circles). The similar velocity distribution between the gas and dwarf satellites in the CGM of M31 is striking, adding more weight that the absorption features at  $-300 \lesssim v_{\text{LSR}} \lesssim -150 \text{ km s}^{-1}$  are indeed probing the CGM gas of M31. This comparison also suggests that the absorption features at  $-420 \lesssim v_{\text{LSR}} \lesssim -300 \text{ km s}^{-1}$  could arise in part from the CGM of M31. However, the other properties of this component are more similar to those seen in the MS; we therefore treat this possible component of the M31 CGM largely contaminated by the MS.

### 3.2.2. Column Densities and Detection Rates versus $R$

In Fig. 5, we show the total column densities of the components at  $-300 \lesssim v_{\text{LSR}} \lesssim -150 \text{ km s}^{-1}$  for C II, Si II, Si III, Si IV, C IV, and O VI as a function of the projected distances from M31,  $R/R_{\text{vir}}$  (using the values listed in Table 2). For all the species, we observe a decrease in the column densities as  $R$  increases. We stress that this relationship between  $N$  and  $R$  seen in all the ions is not trivial and is extremely unlikely to happen by chance. In Fig. 6, we show the column densities for the same component but now as a function of the angular separation from the LG barycenter ( $\Delta\theta_{\text{LGB}}$ ) (where for the LG barycenter, we use  $l = 147^\circ$  and  $b = -25^\circ$  from Einasto & Lynden-Bell 1982; Blitz et al. 1999). There is



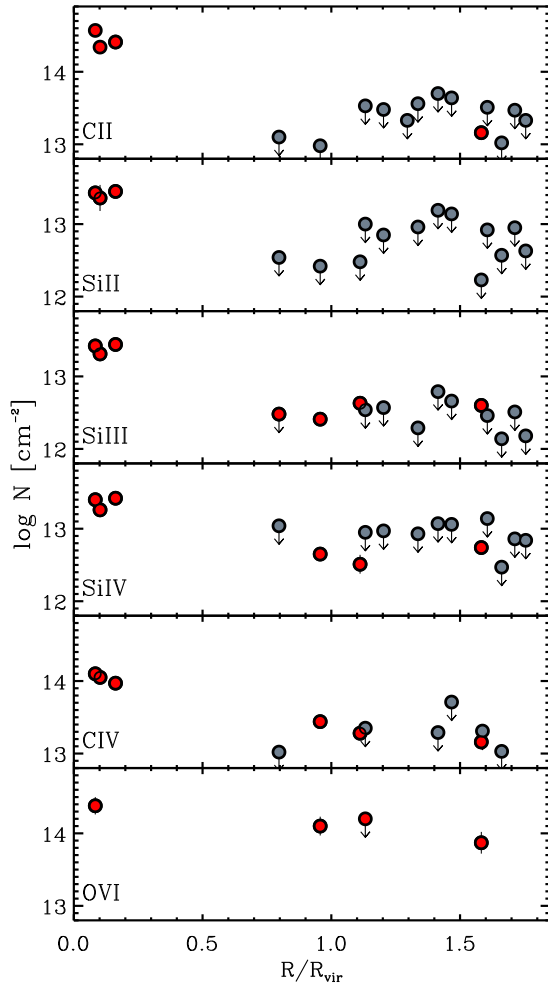


**Figure 5.** Total column density of various ions for the M31 CGM component along each sightline as a function of the impact parameter. Data with no visible error bars mean the errors are smaller than the circles. Gray data with downward arrows are  $3\sigma$  upper limits. Red data with downward arrows indicate that the absorption is detected in a single transition of a single ion.

no relationship between  $N$  and  $\Delta\theta_{\text{LGB}}$ . Although we do not show it here, there is no trend of  $N$  with  $R$  in Si III and C IV for the component at  $-430 \lesssim v_{\text{LSR}} \lesssim -300$   $\text{km s}^{-1}$  (i.e., the MS component).

Using Si III as a sensitive probe of the diffuse ionized gas (e.g., Collins et al. 2009; Shull et al. 2009; Lehner et al. 2012), Fig. 5 also shows that Si III at  $-300 \lesssim v_{\text{LSR}} \lesssim -150$   $\text{km s}^{-1}$  is detected toward all the sightlines within about  $R_{\text{vir}}$ , while only 2 of 11 sightlines beyond  $R_{\text{vir}}$  have a detection of Si III. As we argue in §3.2.1, these two sightlines could be contaminated by the MS. This abrupt change in the detection rate of M31 near  $R_{\text{vir}}$  is again a non-trivial property.

The simplest interpretation of the decrease in the column densities and drop in the detection rate with  $R$  is that the absorption seen at  $-300 \lesssim v_{\text{LSR}} \lesssim -150$   $\text{km s}^{-1}$  traces the CGM of M31.

### 3.2.3. HI Emission and UV Absorption

The CGM of M31 was previously observed in H I 21-cm emission (Thilker et al. 2004; Braun & Thilker

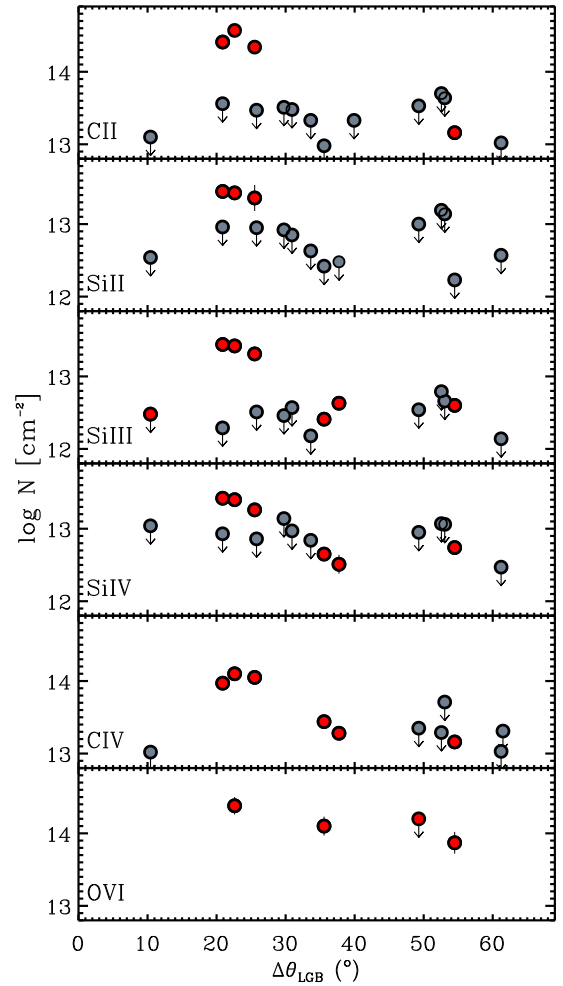


**Figure 6.** Total column density of various ions for the M31 CGM component along each sightline as a function of the angular distance from the Local Group barycenter. Data with no visible error bars mean the errors are smaller than the circles. Gray data with downward arrows are  $3\sigma$  upper limits. Red data with downward arrows indicate that the absorption is detected in a single transition of a single ion.

2004; Westmeier et al. 2005, 2008; Lockman et al. 2012; Wolfe et al. 2013). Several studies have also reported on the H I observations around M33 that occupies the CGM of M31 (Grossi et al. 2008; Putman et al. 2009). The M31 observations found a concentration of H I clouds within 50 kpc of M31 at  $-520 \leq v_{\text{LSR}} \lesssim -150$   $\text{km s}^{-1}$ . For some of these clouds, there is evidence for interaction with M31 or M33 (Thilker et al. 2004; Putman et al. 2009). Both the spatial and kinematic properties of the HVC population around M31 strongly suggest its association with M31 (e.g., Thilker et al. 2004; Westmeier et al. 2008).

From the tabulated velocity components of the H I emission associated with the CGM of M31 by Westmeier et al. (2008) ( $R < 0.2R_{\text{vir}}$ ), Lockman et al. (2012), and Wolfe et al. (2013) ( $R \gtrsim 0.2R_{\text{vir}}$ ), we estimate  $v_{\text{M31}}$  and plot them in Fig. 4 with upside-down triangle symbols. It is apparent that there is also an overlap in the velocities seen in H I emission and UV absorption. While none of our sightlines passes within

the H I cloud contours, some of the H I clouds within  $R < 0.2R_{\text{vir}}$  from M31 and associated with M31 have emission at  $-300 \lesssim v_{\text{LSR}} \lesssim -150 \text{ km s}^{-1}$ , i.e., at velocities seen in the UV absorption (see Fig. 4). Although some H I has been observed at LSR velocities more negative than  $-450 \text{ km s}^{-1}$  ( $v_{\text{M31}} \simeq -200 \text{ km s}^{-1}$ ) near M31 (mostly near the southern edge of M31 where these velocities are expected from the M31 co-rotating disk gas observations by Chemin et al. 2009), we did not find these in the current sample, neither in the inner ( $R \lesssim 0.2R_{\text{vir}}$ ) nor in the distant regions. Rao et al. (2013) found absorption at these velocities along their sightlines near the M31 disk using low resolution COS G140L data, but all their detections are either within or near the disk of M31, all along its major axis (see Fig. 1). We finally note that all but one of the M31 dwarf satellites have also LSR velocities that are not more negative than  $-450 \text{ km s}^{-1}$  (see Table 2 in McConnachie 2012).

### 3.3. Other Origins?

We have presented several properties of the absorption at  $-300 \lesssim v_{\text{LSR}} \lesssim -150 \text{ km s}^{-1}$  that favor an origin in the CGM of M31. As for the H I association with the CGM of M31, we do not rely on a single property to relate this gas to the M31 CGM. It is the combination of the properties laid out in the previous sections that strongly suggests that the gas at  $-300 \lesssim v_{\text{LSR}} \lesssim -150 \text{ km s}^{-1}$  is associated with M31.

We have ruled out that the MS could be the origin of gas at these velocities in the directions of the sightlines in our selected sample. Neither the MW CGM (beyond 20 kpc) nor the LG appears to be a good candidate for the origin of the absorption at  $-300 \lesssim v_{\text{LSR}} \lesssim -150 \text{ km s}^{-1}$ . As shown in the observational cross-correlation of absorbers and galaxies at  $z \lesssim 0.5$  (e.g., Lanzetta et al. 1995; Chen et al. 2001; Wakker & Savage 2009; Prochaska et al. 2011; Werk et al. 2014) and in simulations (e.g., Ford et al. 2014), the column density of metal lines is expected to drop as a function of the impact parameter from the galaxies and the covering fraction is much smaller at  $R > R_{\text{vir}}$  than at  $R < R_{\text{vir}}$ . These properties are observed for the gas at  $-300 \lesssim v_{\text{LSR}} \lesssim -150 \text{ km s}^{-1}$  if it is associated with M31. No trend is observed with the angular separation from the barycenter of the LG (none is really expected, but none is observed by chance either). If we consider any other observed components (MS, MW disk, MW HVCs) and plot the column density of each of these components as a function of the projected distance from M31, no relationship or trend is observed. Finally, the similarity of the velocities for the galaxies associated with M31 and the absorption at  $-300 \lesssim v_{\text{LSR}} \lesssim -150 \text{ km s}^{-1}$  is remarkable. We therefore conclude that the most likely origin of the absorption at  $-300 \lesssim v_{\text{LSR}} \lesssim -150 \text{ km s}^{-1}$  is the CGM of M31 and we now proceed to determine in detail its properties.

## 4. THE PROPERTIES OF THE CGM OF M31

In this section, we derive gas properties (kinematics, ionization, mass) of the uncontaminated component probing the M31 CGM at  $-300 \lesssim v_{\text{LSR}} \lesssim -150 \text{ km s}^{-1}$  (or  $-7 \leq v_{\text{M31}} \leq +110 \text{ km s}^{-1}$  in the M31-centric ve-

locity frame, see Fig 4). As presented in §3.2.1, it is plausible that the M31 CGM gas is also present at  $-450 \lesssim v_{\text{LSR}} \lesssim -300 \text{ km s}^{-1}$  ( $-122 \leq v_{\text{M31}} \leq -34 \text{ km s}^{-1}$ ), but the absorption in this component is very likely largely contaminated by the MS. Hence, there is likely presence of CGM gas at both positive and negative velocities in the M31-centric velocity frames, but we can only determine the properties of the absorption at positive velocities.

### 4.1. Kinematics

Within the uncertainties, the absorption observed in the CGM gas at  $< 0.2R_{\text{vir}}$  is at M31-centric velocities  $+50 \lesssim v_{\text{M31}} \lesssim +100 \text{ km s}^{-1}$ . There is an apparent trend that  $v_{\text{M31}}$  decreases at larger  $R$  where at  $R \geq 0.8R_{\text{vir}}$ ,  $0 \lesssim v_{\text{M31}} \lesssim +30 \text{ km s}^{-1}$ . The velocities toward the 7 targets within  $1.1R_{\text{vir}}$  are within the expected velocities from an extension of a flat rotation curve for M31 to about its virial radius (e.g., Chemin et al. 2009). The remaining target, NGC7469 at  $1.6R_{\text{vir}}$  is at an azimuthal angle similar to some of the other  $R_{\text{vir}}$  targets, and shows absorption at velocities similar to those seen toward these targets. However, as noted in §3, this sightline is the most likely to be contaminated by the MS.

Within the calibration uncertainty of COS ( $\sim 10\text{--}15 \text{ km s}^{-1}$ ), the high and low ions are observed at similar velocities along each sightline. The CGM gas is thus multiphase as observed in the CGM of other galaxies (e.g., Werk et al. 2014; Bordoloi et al. 2014).

In Fig. 4, we also show the expected escape velocity as a function of  $R$  for a  $10^{12} M_{\odot}$  point mass (the dark matter halo of M31 is  $(1.4 \pm 0.4) \times 10^{12} M_{\odot}$ , e.g., van der Marel et al. 2012). All the detected CGM gas is found at velocities below the escape velocity even at large  $R$ . This holds even if we increase  $v_{\text{M31}}$  by  $\sqrt{3}$  to account for unconstrained projection effects. McConnachie (2012) demonstrated that it also holds for most of the galaxies using their 3D distances (instead of the projected distances used here). Therefore, the CGM gas probed in our sample at both small and large  $R$  is gravitationally bound to M31.

### 4.2. Ionization

For the sightlines within  $R < 0.2R_{\text{vir}}$ , there is no strong evidence for significant variation in the ionization levels or gas surface densities since the column densities are similar within  $1\sigma$  for each studied ion (see Table 2 and Fig. 5). However, as shown in Fig. 5 and already noted in §3, the column densities of the M31 CGM component decrease as  $R$  increases for all the ions beyond  $0.2R_{\text{vir}}$ . The gas also becomes more highly ionized as  $R$  increases, as the singly-ionized species are mostly not observed beyond  $0.2R_{\text{vir}}$  (although note the lack of data between 0.2 and  $0.8R_{\text{vir}}$ ), while the higher ions (Si III, Si IV, C IV, O VI) are detected to  $\sim R_{\text{vir}}$  and possibly at  $1.6R_{\text{vir}}$ . The drop in column density between  $0.2R_{\text{vir}}$  and  $\geq 0.8R_{\text{vir}}$  is a factor  $\sim 10$  for Si III, at least a factor 10 for the singly ionized species, a factor  $\sim 5$  for Si IV and C IV, and a factor  $\sim 2$  for O VI. There is no detection of singly ionized species beyond  $0.2R_{\text{vir}}$ , except possibly at  $1.6R_{\text{vir}}$  toward NGC7469 (which is possibly some MS gas, see §3).

The gas is therefore more highly ionized at larger  $R$  than in the inner region. This can be directly quantified using the ratios of several ions of the same element. At  $R < 0.2R_{\text{vir}}$ , we find  $N_{\text{CII}}/N_{\text{CIV}} \gtrsim 2\text{--}3$  and  $N_{\text{SiII}} \sim N_{\text{SiIII}} \sim N_{\text{SiIV}}$ ; however, at  $R > 0.8R_{\text{vir}}$ , we estimate  $N_{\text{CII}}/N_{\text{CIV}} \lesssim 1$  and  $N_{\text{SiII}}/N_{\text{SiIV}} < 0.6$ . We also note that the observed ratio  $N_{\text{CIV}}/N_{\text{SiIV}} \sim 5$  throughout the CGM of M31 is on the high end of those observed in the MW disk and halo gas (e.g., Lehner et al. 2011; Wakker et al. 2012).

We can directly limit the fractional ionization of the gas by comparing the O I column to the column densities of Si II, Si III, and Si IV (Lehner et al. 2001; Zech et al. 2008). O I is an excellent proxy of H I since they have nearly identical ionization potentials and are strongly coupled through charge exchange reactions (Field & Steigman 1971). O and Si have also the same nucleosynthetic origin (they are both  $\alpha$ -elements) and have similar levels of dust depletion in the diffuse gas (Savage & Sembach 1996; Jenkins 2009). Whereas O I arises only in neutral gas, Si II is found in both neutral and ionized gas and Si III and Si IV arise only in ionized gas. Therefore a subsolar ratio of  $[\text{O I}/\text{Si}] = \log(N_{\text{OI}}/N_{\text{Si}}) - \log(\text{O}/\text{Si})_{\odot}$  is expected if the ionization is important.<sup>6</sup> Except for HS0033+4300 and UGC12163, the S/N of the data allows us to place stringent limits on the column density of O I.

Using the results listed in Table 2 we find:  $[\text{O I}/\text{Si}] < -1.4$  and  $< -1.1$  toward RXJ0048.3+3941 and HS0058+4213 at  $R < 0.2R_{\text{vir}}$ ,  $[\text{O I}/\text{Si II}] < -0.1$  toward 3C66A at  $0.8R_{\text{vir}}$ ,  $[\text{O I}/\text{Si}] < -0.6$  toward MRK335 and  $< -0.5$  toward PG0003+158 at about  $R_{\text{vir}}$ , and  $[\text{O I}/\text{Si}] < -0.9$  toward NGC7469 at  $1.6R_{\text{vir}}$ . This implies hydrogen ionization fractions  $\geq 93\text{--}97\%$  at  $R < 0.2R_{\text{vir}}$ . It is very likely that the large impact parameter regions are almost entirely ionized too, especially since the mixture of gas-phases favors the more highly ionized phases. However, the weaker absorption at larger  $R$  produces less stringent limits on the ionization fraction. The CGM gas of M31 is therefore mostly ionized toward all the targets in our sample. It is also more highly ionized at larger  $R$ .

The detections of C IV and O VI are also particularly important since they provide some evidence for  $\sim 10^5$  K gas. It is also an indirect evidence for an extended corona around M31 if thermal instabilities in the hot corona are important or the high ions are at the interface between cool and hot gas. For example, thermal instabilities in a hot corona can produce a warm multiphase, extended CGM if the thermal instability growth time is a factor  $\lesssim 10$  times smaller than the free-fall time of the hot gas (McCourt et al. 2012; Sharma et al. 2012). We also note there is detection of O VI ( $\log N_{\text{OVI}} \simeq 13.9\text{--}14.1$ ) toward MRK352, PG0052+251, and MRK357 at LSR velocities of about  $-190$  km s<sup>-1</sup> (see the component marked ‘‘LG’’ in Table 1 of Sembach et al. 2003), possibly consistent with an origin from the M31 CGM. These targets are at  $14^{\circ} \lesssim \text{RA} \lesssim 21^{\circ}$ ,  $23^{\circ} \lesssim \text{DEC} \lesssim 32^{\circ}$ , and probe the M31 CGM at  $0.4 < R/R_{\text{vir}} < 0.9$ . They are not in our sample because only *FUSE* data exist (see §2). Future COS

observations of these targets would be extremely valuable to confirm such an interpretation. The hot corona also provides an alternative explanation for the existence of H I clouds in the CGM of M31 to that proposed by Wolfe et al. (2013) where they argued that the H I clouds are embedded in an intergalactic filament.

#### 4.3. Covering fractions

Within  $R_{\text{vir}}$ , the covering fraction for Si III and the high ions is close to unity. Each sightline shows Si III absorption from the M31 CGM gas, and hence the covering fraction is 100% ( $> 70\%$  at the 68% confidence level for a sample size of 5) for a  $3\sigma$  sensitivity limit of  $\log N_{\text{SiIII}} \simeq 12.4$  (assuming FWHM  $\simeq 40$  km s<sup>-1</sup>). For C IV, 4/5 of the sightlines show absorption down to a sensitivity of  $\log N_{\text{CIV}} \simeq 12.9$ , which corresponds to a covering fraction of 80% ( $> 48\%$  at the 68% confidence level for a sample size of 5). For O VI, we have only two targets in the inner-most and outer-most regions, and they all show O VI absorption associated with the M31 CGM gas.

Beyond  $R_{\text{vir}}$ , the covering fraction for Si III and the high ions is much smaller in view of the many non-detections. If we set a  $3\sigma$  sensitivity limit of  $\log N_{\text{SiIII}} \simeq 12.6$  based on the detection of Si III, then the detection is rate is 10–20% for  $1 \lesssim R/R_{\text{vir}} \lesssim 1.8$  ( $< 35\%$  at the 68% confidence level for a sample size of 10). For C IV with a sensitivity limit of  $\log N_{\text{CIV}} \simeq 13.3$ , the covering fraction is about 20–30% ( $< 60\%$  at the 68% confidence level for a sample size of 6).

For the singly ionized species, the covering fraction is about 100% for  $R \leq 0.2R_{\text{vir}}$  and  $\ll 1$  at  $R \gtrsim 0.8R_{\text{vir}}$  (see Fig. 5). It would be critical to gain information between  $0.2R_{\text{vir}}$  and  $0.8R_{\text{vir}}$  to determine at which projected distance from M31 the covering fraction of singly ionized species becomes much smaller than 1.

#### 4.4. Metal and Gas Mass

The metal mass of the CGM is independent of the metallicity and can be directly determined from the column densities estimated in Table 2. Following Peeples et al. (2014), the mass of metals in the CGM is  $M_Z = \int 2\pi R \Sigma_Z(R) dR$ . Using Si as a tracer of the metals, the mass surface density of metals is defined as  $\Sigma_Z^{\text{Si}} = \mu_{\text{Si}}^{-1} m_{\text{Si}} N_{\text{Si}}$  where  $\mu_{\text{Si}} = 0.064$  is the solar mass fraction of metals in silicon (i.e.,  $12 + \log(\text{Si}/\text{H})_{\odot} = 7.51$  and  $Z_{\odot} = 0.0142$  from Asplund et al. 2009),  $m_{\text{Si}} = 28m_{\text{p}}$ , and  $N_{\text{Si}} = N_{\text{SiII}} + N_{\text{SiIII}} + N_{\text{SiIV}}$ . We use Si here because we have information on its 3 dominant ionization stages in the  $T < 7 \times 10^4$  K ionized gas, requiring no assumptions on the ionization of the cool gas.

We first consider the region  $R < 0.2R_{\text{vir}}$  where we noted in §4.2 that the column densities for each ion toward the 3 sightlines in this region do not vary much (see Fig. 5). Using the column densities summarized in Table 2 and averaging the values for Si II, Si III, and Si IV for sightlines at  $R < 0.2R_{\text{vir}}$ , we find  $\langle N_{\text{Si}} \rangle = 7.4 \times 10^{13}$  cm<sup>-2</sup>. The mass surface density of metals in the CGM of M31 is then:

$$\log \frac{\Sigma_Z^{\text{Si}}}{\text{M}_{\odot} \text{kpc}^{-2}} = 2.6,$$

which is similar to the observed range of metal surface

<sup>6</sup> We also note that in regions with significant dust, the gas-phase O/Si is expected to be supersolar.

densities found for  $z \sim 0.2$   $L^*$  galaxies ( $\log \Sigma_Z = 3.2$ – $2.0$  at  $R = 26$ – $50$  kpc Peeples et al. 2014). Assuming a covering fraction of 100% based on the detections of Si II, Si III, Si IV in the spectra of the 3 targets in our sample, the CGM metal mass of M31 within  $R \leq 0.2R_{\text{vir}}$  ( $R \leq 50$  kpc) is

$$M_Z^{\text{Si}} = 2.1 \times 10^6 M_{\odot}.$$

This is a factor  $\sim 25$  smaller times than the dust mass in the disk of M31,  $M_{\text{d}}(\text{disk}) = 5.4 \times 10^7 M_{\odot}$  (Draine et al. 2014). The corresponding total gas mass of the CGM of M31 within 50 kpc can be estimated from the metal mass as:

$$M_{\text{g}} = 1435 M_{\text{Si}} \left( \frac{Z_{\odot}}{Z} \right) = 2.9 \times 10^9 \left( \frac{Z_{\odot}}{Z} \right) M_{\odot}.$$

Although we do not know the metallicity  $Z/Z_{\odot}$  of the M31 CGM gas, it is unlikely to be much larger than solar. For the dense region of the CGM of galaxies at  $z \lesssim 1$ , Lehner et al. (2013) found that metallicities range between about  $\lesssim 0.01Z_{\odot}$  and  $\sim 3Z_{\odot}$ , the highest metallicities being associated only with massive outflows (Tripp et al. 2011). In the disk of M31, Sanders et al. (2012) found a scatter between  $0.3 \lesssim Z/Z_{\odot} \lesssim 4$ . The highest allowed metallicity values could therefore not decrease the mass by more than a factor  $\sim 3$ – $4$ . On the other hand, the total mass could be much larger if the metallicity is sub-solar. Within  $0.2R_{\text{vir}}$ , the gas mass in the CGM of M31 is therefore comparable to that in its disk, since  $M_{\text{g}}(\text{disk}) \approx 6 \times 10^9 M_{\odot}$  using the recent results from Draine et al. (2014).

This mass does not include the more highly ionized gas traced by O VI and C IV. If we use C IV (where  $\mu_{\text{C}} = 0.23$ , Asplund et al. 2009) and assume an ionization fraction of  $f_{\text{CIV}} = 0.3$  (which is an upper limit on  $f_{\text{CIV}}$  in collisionally or photoionized gas, see e.g., Gnat & Sternberg 2007; Oppenheimer & Schaye 2013), we find  $M_Z^{\text{CIV}} \geq 1.4 \times 10^6 (0.3/f_{\text{CIV}})(R/50 \text{ kpc})^2 M_{\odot}$ , i.e., the highly ionized CGM gas has a similar mass as the cool photoionized CGM gas.

The current sample of sightlines is too small to determine how the mass changes with radius or azimuth angle. There is also some uncertainty at  $R \gtrsim R_{\text{vir}}$  owing to a plausible contamination from the MS (see §3). Nevertheless, there is undoubtedly a sharp decrease in the column densities at  $R \gtrsim R_{\text{vir}}$  compared to  $R < 0.2R_{\text{vir}}$ , and this drop in  $N$  would be even larger if there is some contamination from the MS. This is displayed in Fig. 5 for all the ions and in Fig. 7, where we show the total column density of Si (where  $\text{Si} = \text{Si II} + \text{Si III} + \text{Si IV}$ ) as a function of  $R/R_{\text{vir}}$ . For the data at  $R \geq 0.8R_{\text{vir}}$ , the vertical bars include the range of possible values if the non-detections are either near their  $3\sigma$  limits or so low as to be negligible (see Table 2 and figures in the Appendix). With no information between the inner and outer regions of the CGM, a linear fit provides the simplest model for characterizing this observed change in the column density of Si with  $R$ , which yields  $N_{\text{Si}}(R) = 10^{12.9} (R/R_{\text{vir}})^{-0.9} \text{ cm}^{-2}$ . This fit is of course poorly constrained and would require more data to model accurately  $N(R)$  and hence  $M(R)$ . In Fig. 7, we also overlay the COS-Halos results from Werk et al. (2014). The experiments that led to these results are very different since for COS-Halos, there is

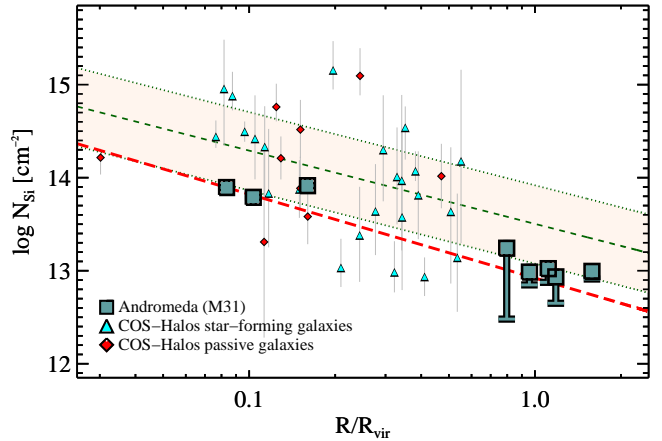


**Figure 7.** Comparison of the total column density of Si versus the impact parameters from M31 and the COS-Halos galaxies from Werk et al. (2014). For the COS-Halos data, the vertical error bar shows the range allowed by the Cloudy photoionization model (see Werk et al. 2014). For M31, the values of  $N_{\text{Si}}$  are directly constrained by our estimates on  $N_{\text{SiII}}$ ,  $N_{\text{SiIII}}$ , and  $N_{\text{SiIV}}$  from the observations; the error bars are less than the size of the square and the vertical blue bars at large impact parameters include the range of possible values if the non-detections are either near their  $3\sigma$  limits or so low as to be negligible. The power-law fit from a linear regression analysis to the data is shown as a green dashed line for the COS-Halos sample (with the light beige shaded area representing the  $1\sigma$  uncertainty in the fit parameters) and a red dashed line for the M31 sample.

one data point per galaxy while there are 7 measurements (and more including the non-detections) for M31. Even given this difference, similar trends are observed. The column densities for M31 are systematically on the low side of the COS-Halos distribution, possibly because some of the absorption may be blended, in particular, with the MS absorption, and hence not taken into account in the total column density (see §3.2.1). For example, making the unreasonable assumption that all the observed absorption arises from the M31 CGM toward HS0058+4213 at  $R \sim 0.2R_{\text{vir}}$ , we find  $\log N_{\text{Si}} > 14.8$ . It is quite plausible that the total column density of Si for the M31 CGM lies between that limit and 13.9 dex, a range of values consistent with COS-Halos.

To estimate the mass within the volume at  $R_{\text{vir}}$ , we use the result from our fit to integrate  $M(R)$  to  $R_{\text{vir}}$ . We find  $M_Z^{\text{Si}}(R_{\text{vir}}) \sim 1.4 \times 10^7 M_{\odot}$  and  $M_{\text{g}}(R_{\text{vir}}) \sim 2.1 \times 10^{10} M_{\odot}$ . As we saw above, the mass of the highly ionized gas is about of the same order. It is also likely that this represents only a lower limit to the total mass of the M31 CGM gas since some of the absorption is likely contaminated by the Magellanic Stream (see §3.2.1). As the stellar mass of M31 is  $10^{11} M_{\odot}$  (e.g., Geehan et al. 2006; Tamm et al. 2012), the mass of the diffuse weakly and highly ionized CGM of M31 is therefore a substantial fraction of the total baryonic mass of M31.

## 5. DISCUSSION

Prior to this work, the CGM of M31 beyond its optical radius has been only explored with deep H I 21-cm emission observations at a sensitivity of  $\log N_{\text{HI}} \geq 17$  (Thilker et al. 2004; Braun & Thilker 2004; Lockman et al. 2012; Wolfe et al. 2013). Within about 50 kpc ( $0.2R_{\text{vir}}$ ), Thilker et al. (2004) found low  $N_{\text{HI}}$  filamentary gas within  $\sim 80 \text{ km s}^{-1}$  of M31 systemic veloc-

ity, i.e., with a velocity separation similar to that seen in the UV data presented here (see Fig 4). They derived a total mass for the H I gas observed through the GBT 9'1 beam of  $3\text{--}4 \times 10^7 M_\odot$ . At  $R > 50$  kpc, the 49' Westerbork H I survey by Braun & Thilker (2004) suggested a filament of H I gas between M31 and M33, but this structure has dissolved into very small clouds of diameters less than a few kpc and masses of a few  $10^5 M_\odot$  when observed with the GBT (Lockman et al. 2012; Wolfe et al. 2013). While the H I mass is still poorly constrained, it is evident the mass of the M31 CGM is dominated by the diffuse ionized gas (see §4.4). Our sample is still small within  $R_{\text{vir}}$ , but each sightline with its pencil beam shows detection of M31 CGM gas for at least Si III, with most showing absorption from multiple ions (Si II, Si III, Si IV, C II, C IV, O VI). It would be of course important to fill the radial and azimuthal spaces with more COS observations of QSOs behind the CGM of M31 in order to confirm these results and more accurately characterize its physical structure. Nevertheless the present observations provide already strong evidence that the CGM of M31 is filled with multiphase, diffuse ionized gas (see §4.3). We do not detect any O I absorption in any of the QSO spectra piercing the CGM of M31, which puts stringent limits on the ionization level,  $\text{H II}/\text{H I} \gtrsim 93\text{--}97\%$  (see §4.2), consistent with the small covering fraction of H I detectable with 21-cm emission observations. Although deep H I emission observations with  $\log N_{\text{HI}} > 17$  reveal only the tip of the iceberg of the CGM, it will be critical that future radio H I surveys can achieve this type of sensitivity with a good angular resolution in order to bring to light the spatial distribution of the H I gas beyond the optical radii of galaxies. The present COS UV sample provides therefore the first strong evidence in the LG for CGM gas beyond 50 kpc (see Lehner et al. 2012).

As displayed in Fig. 3, the associated components with the CGM of M31 are found at  $-300 \lesssim v_{\text{LSR}} \lesssim -150$   $\text{km s}^{-1}$  ( $-7 \leq v_{\text{M31}} \leq +110$   $\text{km s}^{-1}$ ). As shown in Fig. 4, the comparison with the velocity distribution of the dwarf satellites suggests that some of the absorption observed at  $-121 \leq v_{\text{M31}} \leq -34$   $\text{km s}^{-1}$  ( $-450 \lesssim v_{\text{LSR}} \lesssim -300$   $\text{km s}^{-1}$ ) is a mixture of the MS and M31 CGM components, where the absorption is dominated by the MS (see §3.2.1). We also find that  $\sqrt{3}v_{\text{M31}} < v_{\text{esc}}$  (see Fig. 4 and §4.1), implying that the gas is bound to M31 even at large  $R$ .

These results could suggest that the CGM of the MW might be similarly large, but to characterize it will be difficult, since in view of our findings for the M31 CGM, the MW CGM absorption may also be dominated by low-velocity halo clouds (LVHCs,  $|v_{\text{LSR}}| \lesssim 90$   $\text{km s}^{-1}$ ), where the absorption is strongly blended with the MW disk and low halo. Except for the MS, most of the HVCs and iHVCs have been indeed found to be within 5–15 kpc (see, e.g., Thom et al. 2008; Wakker et al. 2008; Lehner & Howk 2011; Lehner et al. 2012, and also Richter 2012 who found a characteristic radial extent of 50 kpc for the H I HVCs of the MW and M31 using a model with a radial exponential decline of the mean H I volume-filling factor). The LVHCs may be the best candidate for an extended MW CGM (Peek et al. 2009),

along with some of the very high-velocity clouds not associated with the MS (Lehner et al. 2012).

We determine that the baryonic mass of the weakly and highly ionized CGM gas of M31 is at least about 30% of the total baryonic mass of M31 (see §4.4), but this does not include the hot  $\geq 10^6$  K CGM coronal component. The ubiquitous detection of high ions in our sample suggests the presence of hot ( $> 10^6$  K) diffuse gas surrounding M31 within its virial radius and possibly beyond (see §4.2) if the production mechanisms of the high ions are dominated by thermal instabilities in the hot corona or interfaces between the cool (Si II, Si III) and putative hot gas (see §4.2). In cosmological simulations, substantial amounts of O VI are produced through collisional ionization in the CGM of galaxies as it transitions from cooling of hot gas (Oppenheimer et al. 2012; Cen 2013; Ford et al. 2013, 2014), although some of the O VI could be photoionized in very low densities at impact parameters  $\geq 100$  kpc ( $\geq 1/3R_{\text{vir}}$ ) (Ford et al. 2014). Cen (2013) show that collisional ionization dominates the production of strong ( $N_{\text{OVI}} > 10^{14}$   $\text{cm}^{-2}$ ) O VI absorbers. For M31 we only find  $N_{\text{OVI}} < 10^{14}$   $\text{cm}^{-2}$  beyond  $R_{\text{vir}}$  (see Fig. 5 and §4.2).

The hot galaxy coronae are one of the fundamental predictions of galaxy formation models (White & Rees 1978; White & Frenk 1991), but their direct detection has been very difficult. Progress has been made recently with the detection of diffuse X-ray emission that appears to extend to about 30–70 kpc around a handful of massive, non-starbursting galaxies (Anderson & Bregman 2011; Bogdán et al. 2013a,b) or in stacked images of galaxies (Anderson et al. 2013). The mass estimate for these hot halos at these radii are about a few times  $10^9 M_\odot$ , which is comparable to the mass found in the cooler ( $< 10^5$  K) gas of the CGM of M31 (see §4.4), and hence the total mass of the CGM of M31 including all the gas-phases could be as large as  $\sim 10^{10} M_\odot$  within 50 kpc. Beyond 50 kpc, the CGM is too diffuse to be traced with X-ray imaging, even though a large mass could be present. Extrapolating to about the virial radius, Anderson & Bregman (2011) estimate that the hot halo mass of the massive spiral galaxy NGC1961 might be about  $10^{11} M_\odot$  (the stellar mass of NGC1961 is  $\sim 3$  times that of M31), a factor 5 larger than the mass of the cool CGM of M31 for the volume within  $R_{\text{vir}}$  (see §4.4). For the MW, Gupta et al. (2012) argue that the mass of the  $2 \times 10^6$  K CGM out to 160 kpc could be as high as  $10^{11} M_\odot$ . However, there is still a large disagreement on the interpretation of the X-ray observations and their implications for an extended hot MW CGM (Gupta et al. 2012, 2014; Wang & Yao 2012; Henley & Shelton 2014; Sakai et al. 2014). The most recent estimate for the MW implies a smaller mass for the  $2 \times 10^6$  K MW CGM gas of about  $4 \times 10^{10} M_\odot$  within 50 or 240 kpc (Miller & Bregman 2015). Based on these X-ray observations, a substantial mass of the M31 CGM could also be present in its hot ( $> 10^6$  K) diffuse corona.

Our results echo the findings from the COS-Halos survey of  $L^*$  galaxies at  $z \sim 0.2$  (Tumlinson et al. 2011; Werk et al. 2013, 2014; Peebles et al. 2014). In Figs. 7 and 8, we reproduce two COS-Halos figures with our M31 results included. Fig. 7 was already presented in §4.4, which shows a similar distribution for  $N_{\text{Si}}$  as a function



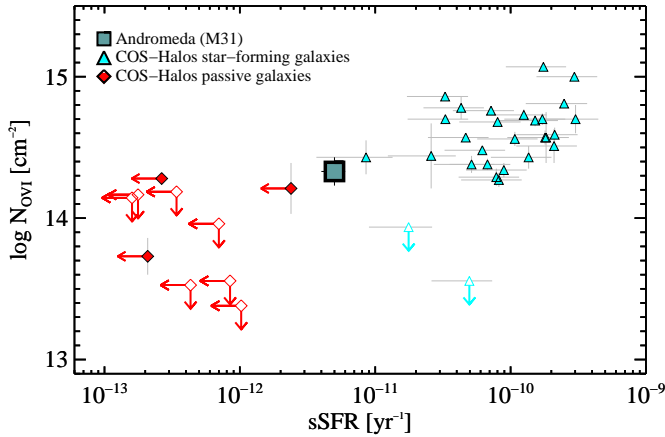


**Figure 8.** Comparison of the total column density of O VI versus the specific star-formation rate of the galaxy between M31 and the COS-Halos program (Tumlinson et al. 2011). For M31, we only consider the sightline with  $R = 25$  kpc since the COS-Halos targeted galaxies with  $R \leq 150$  kpc.

of  $R/R_{\text{vir}}$  between the COS-halos and the present study, which implies similar masses for their cool (probed by Si II, Si III, Si IV) and warm-hot (probed by C IV and O VI) ionized CGM. The typical dark matter halos of the COS-Halos galaxies is  $10^{12} M_{\odot}$ , similar to M31 (e.g., van der Marel et al. 2012). In Fig. 8, we show  $N_{\text{OVI}}$  against the specific star-formation rate of the COS-Halos galaxies and M31.<sup>7</sup> M31 is right between the COS-Halos passively-evolving and star-forming galaxies where star-forming systems have typically  $\log N_{\text{OVI}} \gtrsim 14.3$ . The column density of O VI through the M31 CGM is therefore consistent with the transition observed between the COS-Halos passively-evolving and star-forming galaxies, providing additional evidence – independent of that based on its colors – that M31 might be indeed transitioning from a blue to a red galaxy (Mutch et al. 2011; Dalcanton et al. 2012). We emphasize that although the mass and luminosity of M31 are comparable to the COS-Halos galaxies, their environments might be quite different: M31 lives in a galaxy environment with close by companions (M32, M33, MW, etc.) while the COS-halos galaxies were selected to be fairly isolated. The influence of the MW (750 kpc from M31) on the CGM within 300 kpc of M31 may be thus be relatively small. While the M31 CGM has properties similar to other  $L^*$  galaxies, we find CGM masses at least about 5–6 times larger than estimated for the sub- $L^*$  galaxies at  $z \sim 0$  (Bordoloi et al. 2014).

The origin of this diffuse ionized CGM gas is an open question. The distribution and composition of the CGM gas have been addressed in several high-resolution cosmological hydrodynamic simulations with various level of star formation and feedback prescriptions (e.g., Klypin et al. 2002; Joung et al. 2012; Cen 2013; Nuza et al. 2014; Ford et al. 2014). Notably, despite the various treatments and different levels of the feedback in these simulations, there is some agreement regarding the distribution of the baryons in the CGM between these

<sup>7</sup> As for Si, the total amount of O VI could be larger if some of the O VI absorption of the CGM of M31 is blended with the MS or the MW. However, for O VI, the total column would only increase by about 0.3 dex.

simulations and with our empirical results as we now outline.

One of the basic requirement of all these simulations is that a large fraction of the baryons are in the CGM of galaxies. For example, the  $\Lambda$ CDM-models of the Milky and M31 by Klypin et al. (2002) requires that 1/4 to 1/2 of the baryons within the virial radius of the halo must not be in the disk or bulge of the MW and M31 in the absence of any feedback, which is consistent with our empirical results (see §4.4). Cen (2013) predicts that over half of the gas mass within 150 kpc of red or blue galaxies is in the cool phase of the CGM. Nuza et al. (2014) studied the gas properties in the CGM of MW and M31 analogs using a cosmological simulation of the LG. They find masses for the cool CGM within  $0.2R_{\text{vir}}$  and  $R_{\text{vir}}$  that are consistent with our results. The covering fraction of the CGM gas with  $\log N_{\text{HI}} > 15$  (i.e., tracing some of the ionized gas reported in our work) in their simulation appears also to be broadly consistent with our observations, being close to 1 at  $R \lesssim 0.4R_{\text{vir}}$  and then progressively decreasing to  $\lesssim 0.3$  at  $R \gtrsim R_{\text{vir}}$ . It is worth noting also that in their simulation as well as the more general simulations of galaxies at  $z \sim 0$  (e.g., Cen 2013; Ford et al. 2014), the cool CGM dominates the mass of the CGM within  $0.2R_{\text{vir}}$  (by a factor  $\sim 4$  relative to the mass of the hot gas), but there is a turnover at larger radii where at  $R_{\text{vir}}$  the mass of the hot gas is a factor 3 larger than the mass of the cool gas. While we cannot observe the hot gas associated with the CGM of M31, we find that the gas becomes more ionized and more highly ionized at  $R > 0.8R_{\text{vir}}$  than at  $R < 0.2R_{\text{vir}}$  (see §4.2). Ford et al. (2014) specifically investigated the distribution of similar ions studied in our work and find that the covering fractions of the low (e.g., C II) and high (C IV, O VI) ions are all typically high (near 100%) at  $R < 0.2R_{\text{vir}}$  and drops much more rapidly at higher impact parameter for the low ions than the high ions, again consistent with our empirical results (see §4). The similarity in the distribution of the column densities of C IV and Si IV with  $R$  in the simulations of Ford et al. (2014) (see their Fig. 7) and our observations (see Fig. 5) is striking, with a comparable trend and magnitude in the variation of  $N$  with  $R$  (only C IV and Si IV are common in both studies).

In the Nuza et al. and Ford et al. cosmological simulations, the CGM gas belongs to the ambient medium rather than being associated with satellites. Ford et al. (2014) also show most of the metal mass comes from recycled accretion at any  $R$  (i.e., gas that was once ejected in a wind at least once before), but this is different for the baryons where if the total mass at  $R < 0.2R_{\text{vir}}$  is largely dominated by recycled accretion, at  $R > 0.2R_{\text{vir}}$  the ambient gas (i.e., gas is not going to accrete onto a galaxy and that have never been in a wind by  $z \sim 0$ ) dominates the total mass.

This comparison between cosmological models and our observations is extremely encouraging and demonstrates that a larger sample of targets observed with COS that populate in particular the  $0.2 \leq R/R_{\text{vir}} \lesssim 1$  region of the M31 CGM would make M31 a perfect testbed for theories of galaxy formation and evolution. With our present sample, we cannot accurately assess how the surfaces densities of the different ions change with  $R$  (with

an absence of data points at  $0.2 < R/R_{\text{vir}} < 0.8$ ) or azimuthal angle (e.g., to determine how the surface densities and kinematics vary along the major and minor projected axes of M31). This would also help us to better understand the origins of the metals and baryons in the CGM of M31.

## 6. SUMMARY

With *HST*/COS G130M and G160M and *FUSE* archival observations, we compile a sample of 18 sightlines that pierce the CGM of M31, 3 at small ( $R < 0.2R_{\text{vir}}$ ) and 15 at large ( $0.8 \leq R/R_{\text{vir}} \lesssim 2$ ) projected distances to determine the properties of the CGM at various radii. Along these sightlines, the gas seen in absorption at  $-300 \lesssim v_{\text{LSR}} \lesssim -150 \text{ km s}^{-1}$  in the 3/3 inner-region sightlines and in 4/15 outer-region sightlines is neither associated with the MW (its disk or CGM) nor with the MS. These velocities are about  $40\text{--}90 \text{ km s}^{-1}$  from the systemic velocity of M31. Only for this component do we observe a non-trivial relationship between the column densities of the observed ions (Si II, Si III, Si IV, C II, C IV, O VI) and the projected distance from M31 whereby  $N$  decreases with  $R$ . These and other arguments presented in §3 imply that the absorption at  $-300 \lesssim v_{\text{LSR}} \lesssim -150 \text{ km s}^{-1}$  observed in the directions probed by our selected sightlines must in all likelihood arise from the CGM of the M31. We determine the following properties for the CGM of M31 traced by this absorption:

1. The M31 CGM gas is observed at similar velocities to that of the satellites galaxies located in the CGM of M31. These velocities are small enough relative to the escape velocity to conclude that the observed CGM gas is gravitationally bound even at large  $R$ .
2. Low (Si II, C II), intermediate (Si III), and high ions (Si IV, C IV) are all observed in absorption toward the 3 sightlines at  $R < 0.2R_{\text{vir}}$ , while typically only Si III and high ions are observed at  $R \geq 0.8R_{\text{vir}}$ . The CGM gas of M31 is therefore more highly ionized at larger projected distances.
3. Within  $R_{\text{vir}}$ , the covering fraction for Si III and the high ions is close to unity. Beyond  $R_{\text{vir}}$ , the covering fraction for Si III and the high ions drops to  $< 20\%$ . For the singly ionized species, the covering fraction is about 100% for  $R \leq R_{\text{vir}}$  and  $\ll 1$  at  $R \gtrsim 0.8R_{\text{vir}}$ .
4. With sensitive limits on the column density O I and its comparison to the total column density of Si (Si II+Si III+Si IV), we show that the CGM of M31 is predominantly ionized ( $\gtrsim 95\%$ ). The M31 CGM gas is therefore multiphase, dominantly ionized (i.e.,  $\text{H II} \gg \text{H I}$ ), and becomes more highly ionized gas at larger  $R$ . The presence of a large amount of multiphase gas suggests that M31 has very likely a hot corona extending all the way to  $R_{\text{vir}}$  and possibly beyond.
5. We derive using Si II, Si III, and Si IV a CGM metal mass of  $2.1 \times 10^6 M_{\odot}$  and gas mass of  $3 \times 10^9 (Z_{\odot}/Z) M_{\odot}$  within  $0.2R_{\text{vir}}$ , implying a substantial mass of

metal and gas within  $0.2R_{\text{vir}}$ . In the volume within  $R_{\text{vir}}$ , we estimate  $M_{\text{Si}} \sim 1.4 \times 10^7 M_{\odot}$  and  $M_{\text{g}} \sim 2.1 \times 10^{10} M_{\odot}$ ; there is, however, a substantial uncertainty in the masses estimated at  $R_{\text{vir}}$  given the lack of observations between  $0.2 \leq R/R_{\text{vir}} \leq 0.8$ . The highly ionized CGM gas of M31 probed by C IV (and O VI) have most likely similar masses. The baryonic mass of the weakly and highly ionized CGM gas of M31 is about 30% of the total baryonic mass of M31 (not including the hot  $\geq 10^6 \text{ K}$  CGM coronal gas).

6. The above conclusions imply that M31 has an extended, massive, multiphase CGM as observed in higher redshift  $L^*$  galaxies. With the current data, there is a broad agreement between our empirical results and recent cosmological simulations in terms of baryonic mass and change in the ionization levels with projected distances. However, a larger sample will be critical to determine the properties in the  $0.2 \lesssim R/R_{\text{vir}} < 1$  range where currently there is no information. Despite an environment that is different from the isolated galaxies in the COS-Halos survey, the properties of the CGM of M31 is fairly typical of a  $L^*$  disk galaxy that might be transitioning from a blue to red galaxy.

## ACKNOWLEDGEMENTS

We thank Jason Tumlinson and Jessica Werk for sharing the COS-Halos data and the IDL codes that helped producing Figs. 7 and 8. We thank Kate Rubin, Mary Putman, Filippo Fraternali, Prateek Sharma, David Valls-Gabaud, and Daniel Wang for useful suggestions and discussions and the anonymous referee for providing feedback, which helped us to improve the content and clarity of our manuscript. NL and JCH acknowledge support for this research provided by National Science Foundation under grant no. AST-1212012 and NASA through grants HST-GO-12604, HST-AR-12854, and HST-GO-12982 from the Space Telescope Science Institute, which is operated by the Association of Universities for Research in Astronomy, Incorporated, under NASA contract NAS5-26555. BPW acknowledges support from the National Science Foundation under grant no. AST-1108913 and NASA through grant HST-GO-12604 from the Space Telescope Science Institute. All of the data presented in this paper were obtained from the Mikulski Archive for Space Telescopes (MAST). STScI is operated by the Association of Universities for Research in Astronomy, Inc., under NASA contract NAS5-26555. This research has made use of the NASA's Astrophysics Data System Abstract Service and the SIMBAD database, operated at CDS, Strasbourg, France.

## REFERENCES

- Anderson, M. E., & Bregman, J. N. 2011, *ApJ*, 737, 22  
 Anderson, M. E., Bregman, J. N., & Dai, X. 2013, *ApJ*, 762, 106  
 Asplund, M., Grevesse, N., Sauval, A. J., & Scott, P. 2009, *ARA&A*, 47, 481  
 Barger, K. A., Lehner, N., & Howk, J. C. 2014, *ApJ*, submitted  
 Besla, G., Kallivayalil, N., Hernquist, L., et al. 2012, *MNRAS*, 421, 2109  
 Blitz, L., Spergel, D. N., Teuben, P. J., Hartmann, D., & Burton, W. B. 1999, *ApJ*, 514, 818  
 Bogdán, Á., Forman, W. R., Kraft, R. P., & Jones, C. 2013a, *ApJ*, 772, 98

- Bogdán, Á., Forman, W. R., Vogelsberger, M., et al. 2013b, *ApJ*, 772, 97
- Bordoloi, R., Tumlinson, J., Werk, J. K., et al. 2014, *ApJ*, 796, 136
- Braun, R., & Thilker, D. A. 2004, *A&A*, 417, 421
- Brown, T. M., Smith, E., Ferguson, H. C., et al. 2006, *ApJ*, 652, 323
- Brüms, C., Kerp, J., Staveley-Smith, L., et al. 2005, *A&A*, 432, 45
- Cen, R. 2013, *ApJ*, 770, 139
- Chemin, L., Carignan, C., & Foster, T. 2009, *ApJ*, 705, 1395
- Chen, H.-W., Helsby, J. E., Gauthier, J.-R., et al. 2010, *ApJ*, 714, 1521
- Chen, H.-W., Lanzetta, K. M., & Webb, J. K. 2001, *ApJ*, 556, 158
- Churchill, C. W., Kacprzak, G. G., Steidel, C. C., et al. 2012, *ApJ*, 760, 68
- Clemens, D. P. 1985, *ApJ*, 295, 422
- Collins, J. A., Shull, J. M., & Giroux, M. L. 2009, *ApJ*, 705, 962
- Dalcanton, J. J., Williams, B. F., Lang, D., et al. 2012, *ApJS*, 200, 18
- Davidge, T. J., McConnachie, A. W., Fardal, M. A., et al. 2012, *ApJ*, 751, 74
- Dekel, A., & Birnboim, Y. 2006, *MNRAS*, 368, 2
- Draine, B. T., Aniano, G., Krause, O., et al. 2014, *ApJ*, 780, 172
- Einasto, J., & Lynden-Bell, D. 1982, *MNRAS*, 199, 67
- Faucher-Giguère, C.-A., & Kereš, D. 2011, *MNRAS*, 412, L118
- Field, G. B., & Steigman, G. 1971, *ApJ*, 166, 59
- Ford, A. B., Oppenheimer, B. D., Davé, R., et al. 2013, *MNRAS*, 432, 89
- Ford, A. B., Davé, R., Oppenheimer, B. D., et al. 2014, *MNRAS*, 444, 1260
- Fox, A. J., Richter, P., Wakker, B. P., et al. 2013, *ApJ*, 772, 110
- Fox, A. J., Savage, B. D., & Wakker, B. P. 2006, *ApJS*, 165, 229
- Fox, A. J., Wakker, B. P., Barger, K. et al. 2014, *ApJ*, 787, 147
- Garrison-Kimmel, S., Boylan-Kolchin, M., Bullock, J. S., & Lee, K. 2014, *MNRAS*, 438, 2578
- Geehan, J. J., Fardal, M. A., Babul, A., & Guhathakurta, P. 2006, *MNRAS*, 366, 996
- Gilbert, K. M., Guhathakurta, P., Beaton, R. L., et al. 2012, *ApJ*, 760, 76
- Gilbert, K. M., Kalirai, J. S., Guhathakurta, P., et al. 2014, *ApJ*, 796, 76
- Gnat, O., & Sternberg, A. 2007, *ApJS*, 168, 213
- Gordon, K. D., Bailin, J., Engelbracht, C. W., et al. 2006, *ApJ*, 638, L87
- Green, J. C., Froning, C. S., Osterman, S., et al. 2012, *ApJ*, 744, 60
- Grossi, M., Giovanardi, C., Corbelli, E., et al. 2008, *A&A*, 487, 161
- Gupta, A., Mathur, S., Galeazzi, M., & Krongold, Y. 2014, *Ap&SS*, 352, 775
- Gupta, A., Mathur, S., Krongold, Y., Nicastro, F., & Galeazzi, M. 2012, *ApJ*, 756, LL8
- Henley, D. B., & Shelton, R. L. 2014, *ApJ*, 784, 54
- Howk, J. C., Savage, B. D., Sembach, K. R., & Hoopes, C. G. 2002, *ApJ*, 572, 264
- Jenkins, E. B. 2009, *ApJ*, 700, 1299
- Joung, M. R., Putman, M. E., Bryan, G. L., Fernández, X., & Peek, J. E. G. 2012, *ApJ*, 759, 137
- Kacprzak, G. G., Churchill, C. W., Steidel, C. C., Spitler, L. R., & Holtzman, J. A. 2012, *MNRAS*, 427, 3029
- Kacprzak, G. G., Martin, C. L., Bouché, N., et al. 2014, *ApJ*, 792, LL12
- Kalberla, P. M. W., Burton, W. B., Hartmann, D., et al. 2005, *A&A*, 440, 775
- Kang, Y., Bianchi, L., & Rey, S. 2009, *ApJ*, 703, 614
- Keeney, B. A., Stocke, J. T., Rosenberg, J. L., et al. 2013, *ApJ*, 765, 27
- Kereš, D., Katz, N., Weinberg, D. H., & Davé, R. 2005, *MNRAS*, 363, 2
- Klypin, A., Zhao, H., & Somerville, R. S. 2002, *ApJ*, 573, 597
- Lanzetta, K. M., Bowen, D. V., Tytler, D., & Webb, J. K. 1995, *ApJ*, 442, 538
- Lehner, N., & Howk, J. C. 2007, *MNRAS*, 377, 687
- Lehner, N., & Howk, J. C. 2010, *ApJ*, 709, L138
- Lehner, N., & Howk, J. C. 2011, *Science*, 334, 955
- Lehner, N., Howk, J. C., Keenan, F. P., & Smoker, J. V. 2008, *ApJ*, 678, 219
- Lehner, N., Howk, J. C., Thom, C., et al. 2012, *MNRAS*, 424, 2896
- Lehner, N., Howk, J. C., Tripp, T. M., et al. 2013, *ApJ*, 770, 138
- Lehner, N., Keenan, F. P., & Sembach, K. R. 2001, *MNRAS*, 323, 904
- Lehner, N., Staveley-Smith, L., & Howk, J. C. 2009, *ApJ*, 702, 940
- Lehner, N., Zech, W. F., Howk, J. C., & Savage, B. D. 2011, *ApJ*, 727, 46
- Liang, C. J., & Chen, H.-W. 2014, *MNRAS*, 445, 2061
- Lockman, F. J., Free, N. L., & Shields, J. C. 2012, *AJ*, 144, 52
- McConnachie, A. W. 2012, *AJ*, 144, 4
- McConnachie, A. W., Irwin, M. J., Ibata, R. A., et al. 2009, *Nature*, 461, 66
- McCourt, M., Sharma, P., Quataert, E., & Parrish, I. J. 2012, *MNRAS*, 419, 3319
- Miller, M. J., & Bregman, J. N. 2015, *ApJ*, 800, 14
- Moos, H. W., Cash, W. C., Cowie, L. L., et al. 2000, *ApJ*, 538, L1
- Morton, D. C. 2003, *ApJS*, 149, 205
- Mutch, S. J., Croton, D. J., & Poole, G. B. 2011, *ApJ*, 736, 84
- Nidever, D. L., Majewski, S. R., & Burton, W. B. 2008, *ApJ*, 679, 432
- Nuza, S. E., Parisi, F., Scannapieco, C., et al. 2014, *MNRAS*, submitted arXiv:1403.7528
- Oppenheimer, B. D., Davé, R., Katz, N., Kollmeier, J. A., & Weinberg, D. H. 2012, *MNRAS*, 420, 829
- Oppenheimer, B. D., & Schaye, J. 2013, *MNRAS*, 434, 1043
- Peek, J. E. G., Heiles, C., Putman, M. E., & Douglas, K. 2009, *ApJ*, 692, 827
- Peeples, M. S., Werk, J. K., Tumlinson, J., et al. 2014, *ApJ*, 786, 54
- Penton, S. V., Stocke, J. T., & Shull, J. M. 2002, *ApJ*, 565, 720
- Prochaska, J. X., Weiner, B., Chen, H.-W., Mulchaey, J., & Cooksey, K. 2011, *ApJ*, 740, 91
- Putman, M. E., Gibson, B. K., Staveley-Smith, L., et al. 1998, *Nature*, 394, 752
- Putman, M. E., Peek, J. E. G., & Joung, M. R. 2012, *ARA&A*, 50, 491
- Putman, M. E., Peek, J. E. G., Muratov, A., et al. 2009, *ApJ*, 703, 1486
- Rao, S. M., Sardane, G., Turnshek, D. A., et al. 2013, *MNRAS*, 432, 866
- Richter, P. 2012, *ApJ*, 750, 165
- Riess, A. G., Fliri, J., & Valls-Gabaud, D. 2012, *ApJ*, 745, 156
- Ryans, R. S. I., Keenan, F. P., Sembach, K. R., & Davies, R. D. 1997, *MNRAS*, 289, 83
- Sakai, K., Yao, Y., Mitsuda, K., et al. 2014, *PASJ*, 66, 83
- Sanders, N. E., Caldwell, N., McDowell, J., & Harding, P. 2012, *ApJ*, 758, 133
- Savage, B. D., & Sembach, K. R. 1991, *ApJ*, 379, 245
- Savage, B. D., & Sembach, K. R. 1996, *ARA&A*, 34, 279
- Savage, B. D., Sembach, K. R., Wakker, B. P., et al. 2003, *ApJS*, 146, 125
- Sembach, K. R., Wakker, B. P., Savage, B. D., et al. 2003, *ApJS*, 146, 165
- Sharma, P., McCourt, M., Quataert, E., & Parrish, I. J. 2012, *MNRAS*, 420, 3174
- Shull, J. M. 2014, *ApJ*, 784, 142
- Shull, J. M., Jones, J. R., Danforth, C. W., & Collins, J. A. 2009, *ApJ*, 699, 754
- Smoker, J. V., Fox, A. J., & Keenan, F. P. 2011, *MNRAS*, 415, 1105
- Spitzer, L., Jr. 1956, *ApJ*, 124, 20
- Stanimirović, S., Dickey, J. M., Krčo, M., & Brooks, A. M. 2002, *ApJ*, 576, 773
- Stocke, J. T., Keeney, B. A., Danforth, C. W., et al. 2013, *ApJ*, 763, 148
- Tamm, A., Tempel, E., Tenjes, P., Tihhonova, O., & Tuvikene, T. 2012, *A&A*, 546, A4
- Thilker, D. A., Braun, R., Walterbos, R. A. M., et al. 2004, *ApJ*, 601, L39
- Thom, C., Peek, J. E. G., Putman, M. E., et al. 2008, *ApJ*, 684, 364
- Thom, C., Putman, M. E., Gibson, B. K., et al. 2006, *ApJ*, 638, L97
- Thom, C., Tumlinson, J., Werk, J. K., et al. 2012, *ApJ*, 758, LL41
- Thom, C., Werk, J. K., Tumlinson, J., et al. 2011, *ApJ*, 736, 1
- Tripp, T. M., Meiring, J. D., Prochaska, J. X., et al. 2011, *Science*, 334, 952
- Tumlinson, J., Thom, C., Werk, J. K., et al. 2011, *Science*, 334, 948
- Tumlinson, J., Thom, C., Werk, J. K., et al. 2013, *ApJ*, 777, 59
- van der Marel, R. P., Fardal, M., Besla, G., et al. 2012, *ApJ*, 753, 8
- Wakker, B. P. 2001, *ApJS*, 136, 463
- Wakker, B. P. 2006, *ApJS*, 163, 282
- Wakker, B. P., & Savage, B. D. 2009, *ApJS*, 182, 378
- Wakker, B. P., Savage, B. D., Fox, A. J., Benjamin, R. A., & Shapiro, P. R. 2012, *ApJ*, 749, 157
- Wakker, B. P., Savage, B. D., Sembach, K. R., et al. 2003, *ApJS*, 146, 1
- Wakker, B. P., York, D. G., Howk, J. C., et al. 2007, *ApJ*, 670, L113
- Wakker, B. P., York, D. G., Wilhelm, R., et al. 2008, *ApJ*, 672, 298
- Walterbos, R. A. M., & Kennicutt, R. C., Jr. 1987, *A&AS*, 69, 311
- Wang, Q. D., & Yao, Y. 2012, arXiv:1211.4834
- Westmeier, T., Braun, R., & Thilker, D. 2005, *A&A*, 436, 101

Westmeier, T., Brüns, C., & Kerp, J. 2008, MNRAS, 390, 1691  
 Werk, J. K., Prochaska, J. X., Thom, C., et al. 2013, ApJS, 204, 17  
 Werk, J. K., Prochaska, J. X., Tumlinson, J., et al. 2014, ApJ, submitted [arXiv:1403.0947]  
 White, S. D. M., & Rees, M. J. 1978, MNRAS, 183, 341

White, S. D. M., & Frenk, C. S. 1991, ApJ, 379, 52  
 Wolfe, S. A., Pisano, D. J., Lockman, F. J., McGaugh, S. S., & Shaya, E. J. 2013, Nature, 497, 224  
 Zech, W. F., Lehner, N., Howk, J. C., Dixon, W. V. D., & Brown, T. M. 2008, ApJ, 679, 460

## APPENDIX

In this appendix, we show all the absorption profiles used in this work as well as describe in detail each line of sight. Figs. A1 to A18 show the *HST*/COS and *FUSE* absorption-line normalized profiles for the 18 QSO targets in the sample, sorted by increasing projected distances from the center of M31. The red region in each spectrum shows the component that is associated with the CGM of M31 (see §3). Absorption at  $v_{\text{LSR}} > -150$   $\text{km s}^{-1}$  is associated with the MW disk and halo. When detected, the absorption at  $-430 \lesssim v_{\text{LSR}} \lesssim -300$   $\text{km s}^{-1}$  is typically associated with the MS. We now give some additional information on the observed HVC components  $v_{\text{LSR}} \lesssim -170$   $\text{km s}^{-1}$  (i.e., here defined as the gas that is not part of the Milky disk or halo) for each sightline.

- *RXJ0048.1+3941*: In Fig. A1, we show its normalized profiles. HVCs are observed at LSR velocities centered on  $-380, -325$   $\text{km s}^{-1}$  that we associate with the MS extension and  $-242, -182$   $\text{km s}^{-1}$  that we associate with the M31 CGM. We estimate the total column densities of two velocity-components at  $-242$  and  $-182$   $\text{km s}^{-1}$  for the M31 CGM component. Absorption is observed for all the ions but O I in the M31 CGM component.

- *HS0033+4300*: In Fig. A2, we show its normalized profiles. HVCs are observed at LSR velocities centered on  $-375$   $\text{km s}^{-1}$  that we associate with the MS extension and  $-204$   $\text{km s}^{-1}$  that we associate with the M31 CGM. In the M31 CGM component, there might be more than 1 component, but the S/N is too low to discern the exact velocity structure. Absorption is observed for all the ions but O I in the M31 CGM component.

- *HS0058+4213*: In Fig. A3, we show its normalized profiles. An HVC is observed at LSR velocity centered on  $-211$   $\text{km s}^{-1}$  that we associate with the M31 CGM. In the M31 CGM component, there might be more than 1 component, but the S/N is too low to discern the exact velocity structure. No absorption at more negative velocity is observed. Absorption is observed for all the ions but O I in the M31 CGM component.

- *3C66A*: In Fig. A4, we show its normalized profiles. An HVC is observed at LSR velocity centered on  $-256$   $\text{km s}^{-1}$  that we associate with the M31 CGM. Absorption is only observed in Si II  $\lambda 1206$  at nearly  $7\sigma$  ( $W_\lambda = 57.1 \pm 8.4$   $\text{m}\text{\AA}$ ). Because it is observed in only one transition, we report the column density as a lower limit to emphasize that this absorption could be contaminated by an unrelated absorber.

- *PG0003+158*: In Fig. A6, we show its normalized profiles (C II  $\lambda 1334$  is not shown because it is heavily contaminated by unrelated absorbers). Several HVCs are observed at  $v_{\text{LSR}} = -390, -325$   $\text{km s}^{-1}$  that we associate with the possible MS extension and at  $-232$   $\text{km s}^{-1}$  that we associate with the M31 CGM. In the M31 CGM component, no O I or singly ionized species are detected.

- *UGC12163*: In Fig. A7, we show its normalized profiles. Several HVCs are observed in several ions at  $v_{\text{LSR}} = -428, -325$   $\text{km s}^{-1}$  that we associate with the possible MS extension. Absorption at  $-274$   $\text{km s}^{-1}$  is only observed in O VI  $\lambda 1031$  that we associate with the M31 CGM. In this case there is no evidence for MW or MS O VI absorption along this sightline, and hence O VI is not blended as seen in other sightlines. However, because it is observed in only one transition, we report the column density as a lower limit to emphasize that this absorption could be contaminated by an unrelated absorber.

- *MRK1502*: In Fig. A8, we show its normalized profiles where no HVC absorption is observed at the  $3\sigma$  level.

- *MRK1501*: In Fig. A9, we show its normalized profiles where no HVC absorption is observed at the  $3\sigma$  level, but we note the S/N is very low in Si II, Si III, and Si IV.

- *SDSSJ015952.95+134554.3*: In Fig. A10, we show its normalized profiles where no HVC absorption is observed at the  $3\sigma$  level.

- *3C454.3*: In Fig. A11, we show its normalized profiles where no HVC absorption is observed at the  $3\sigma$  level between  $-300$  and  $-150$   $\text{km s}^{-1}$ . There is a strong absorption centered at  $-380$   $\text{km s}^{-1}$  that we associate with the MS.

- *SDSSJ225738.20+134045.0*: In Fig. A12, we show its normalized profiles where no absorption is observed at the  $3\sigma$  level between  $-300$  and  $-150$   $\text{km s}^{-1}$ . There is a strong absorption centered at  $-360$   $\text{km s}^{-1}$  that we associate with the MS.

- *NGC7469*: In Fig. A13, we show its normalized profiles. HVCs are observed at LSR velocities centered on  $-330$   $\text{km s}^{-1}$  that we associate with the MS and  $-239$   $\text{km s}^{-1}$  that we associate with the M31 CGM. We note that an additional HVC is observed centered at about  $-170$   $\text{km s}^{-1}$  and spanning the velocity interval  $[-200, -110]$   $\text{km s}^{-1}$  that is likely associated with the MW halo (see §3).

- *HS2154+2228*: In Fig. A14, we show its normalized profiles. This target was only observed with G160M. The absorption seen in C IV at  $-320$   $\text{km s}^{-1}$  cannot be confirmed because C IV  $\lambda 1550$  is contaminated. We only report a non-detection of C IV in the range  $[-270, -150]$   $\text{km s}^{-1}$ .

- *PHL1226*: In Fig. A15, we show its normalized profiles where no absorption is observed at the  $3\sigma$  level. The strong absorption seen in Si III  $\lambda 1206$  at  $v_{\text{LSR}} < -300$   $\text{km s}^{-1}$  is not confirmed in any other ions and is likely not a MS component (especially since C II absorption is not observed while it is typically observed in the MS component toward other sightlines with similar Si III absorption).

- *MRK304*: In Fig. A16, we show its normalized profiles where no absorption is observed at the  $3\sigma$  level for the M31 CGM component. There is, however, strong absorption in C II, Si III, Si IV, and C IV at  $-340$   $\text{km s}^{-1}$  that we associate with the MS extension.

- *MRK595*: In Fig. A17, we show its normalized profiles where no HVC absorption is observed at the  $3\sigma$  level for the MS or M31 CGM component.

- *MRK1014*: In Fig. A18, we show its normalized profiles where no HVC absorption is observed at the  $3\sigma$  level for the MS or M31 CGM component.

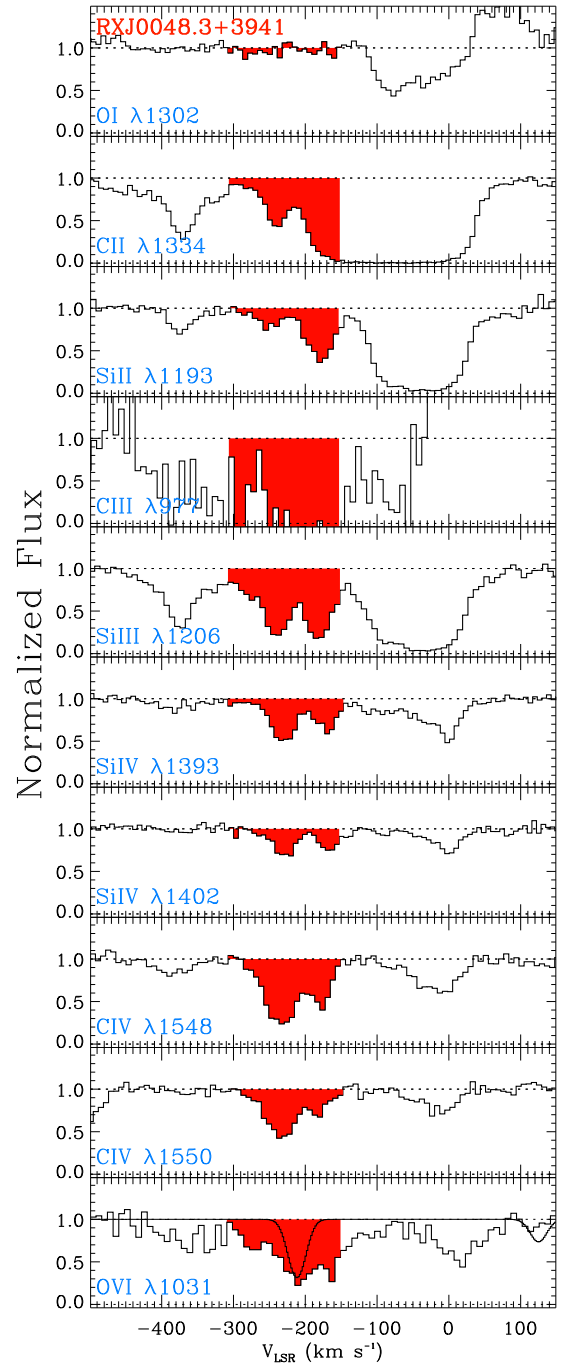


**Figure A1.** Normalized profiles of RXJ0048.1+3941 at  $R = 25$  kpc. The spectra were obtained with COS G130M and G160M, except for C III and O VI, which were obtained with *FUSE*. The red region shows the absorption from the M31 CGM gas. The MW and HVC absorption is at  $v_{\text{LSR}} \gtrsim -170 \text{ km s}^{-1}$ , while the MS absorption is at  $-430 \lesssim v_{\text{LSR}} \lesssim -310 \text{ km s}^{-1}$ . In the O VI panel, we overplot the  $\text{H}_2$  model that was used to correct the O VI absorption from the  $\text{H}_2$  contamination. Note that O I is affected by O I airglow emission line at  $v_{\text{LSR}} \gtrsim -100 \text{ km s}^{-1}$ .



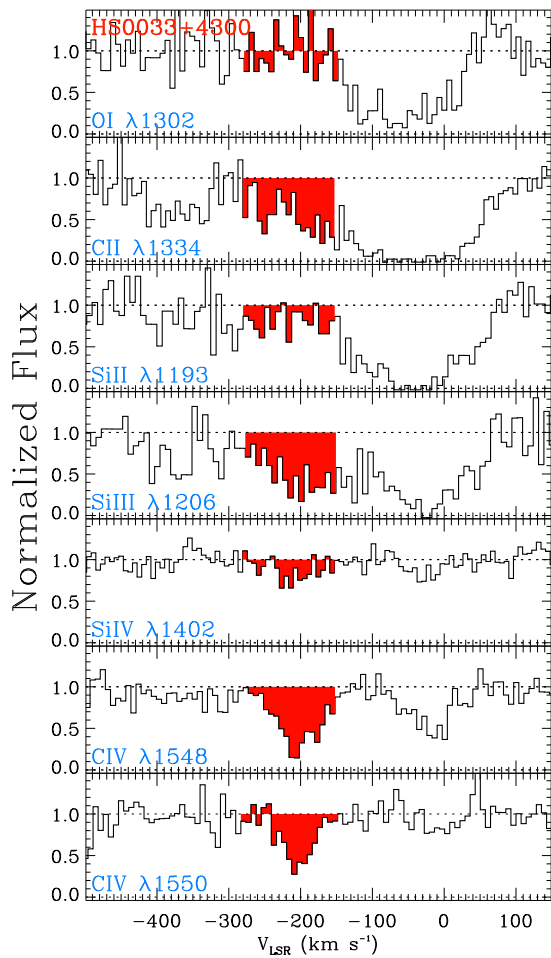


**Figure A2.** Same as Fig. A1, but for HS0033+4300 at  $R = 31$  kpc.

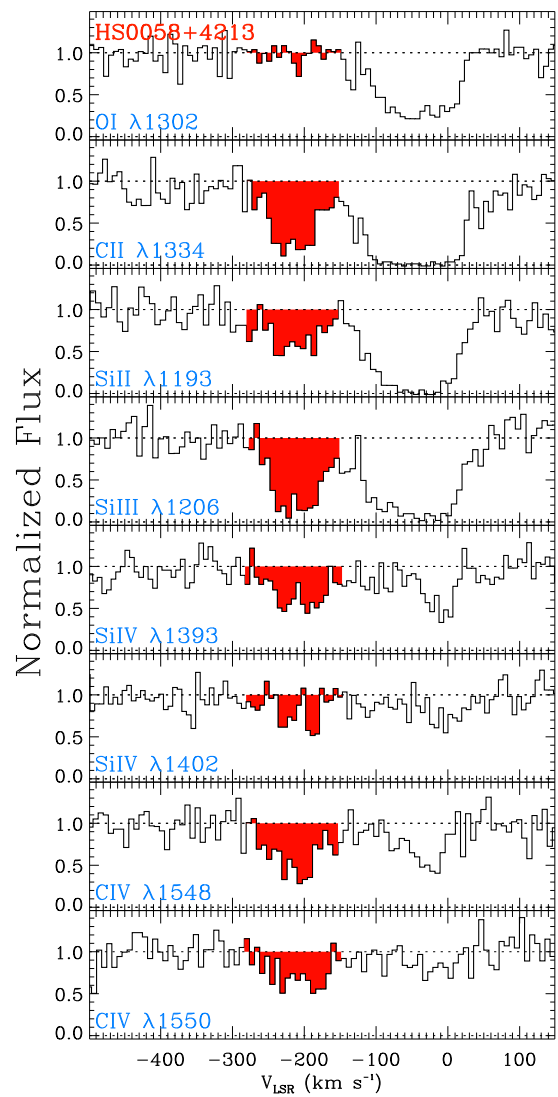


**Figure A3.** Same as Fig. A1, but for HS0058+4213 at  $R = 49$  kpc. There is no evidence of MS absorption toward this sightline.

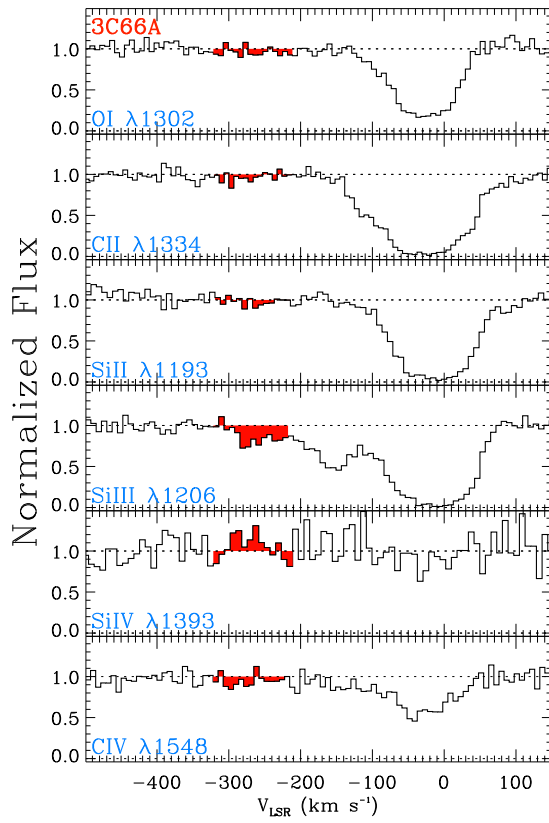


Figure A4. Same as Fig. A1, but for 3C66A at  $R = 239$  kpc.

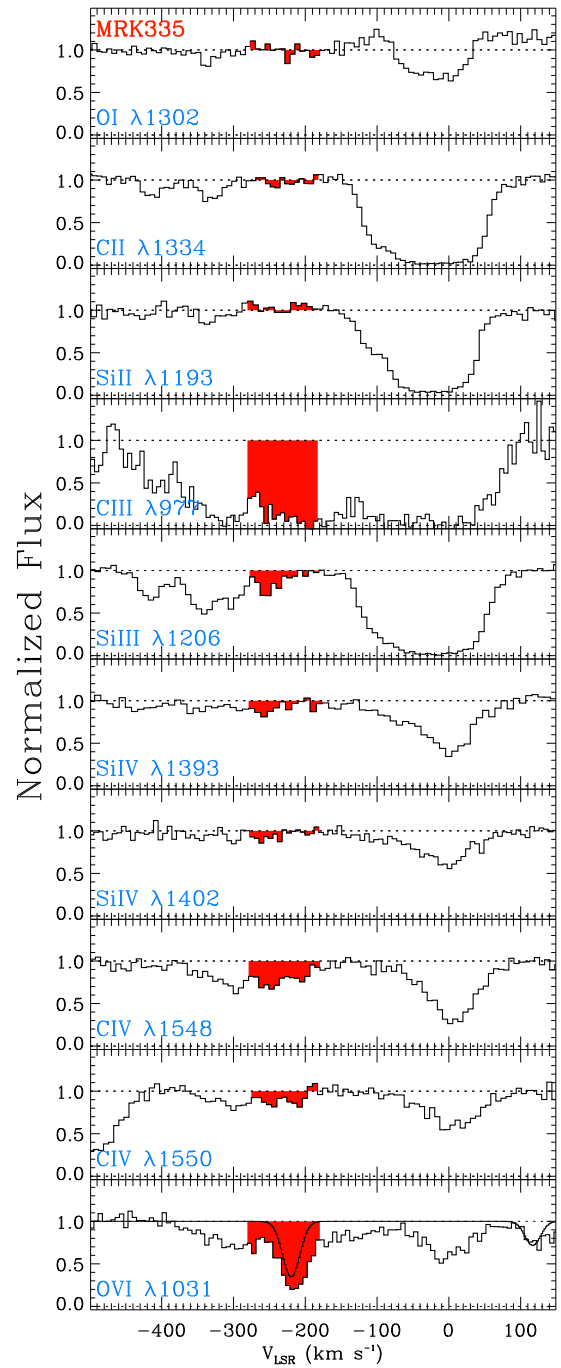
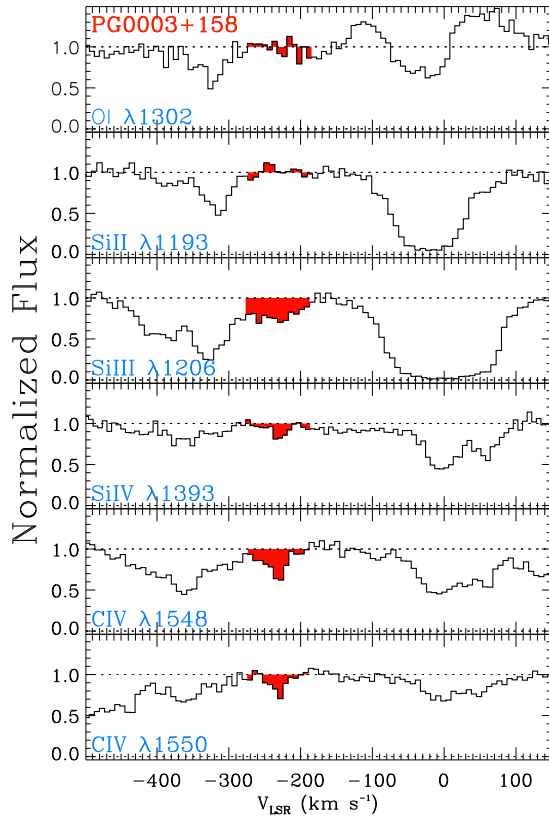
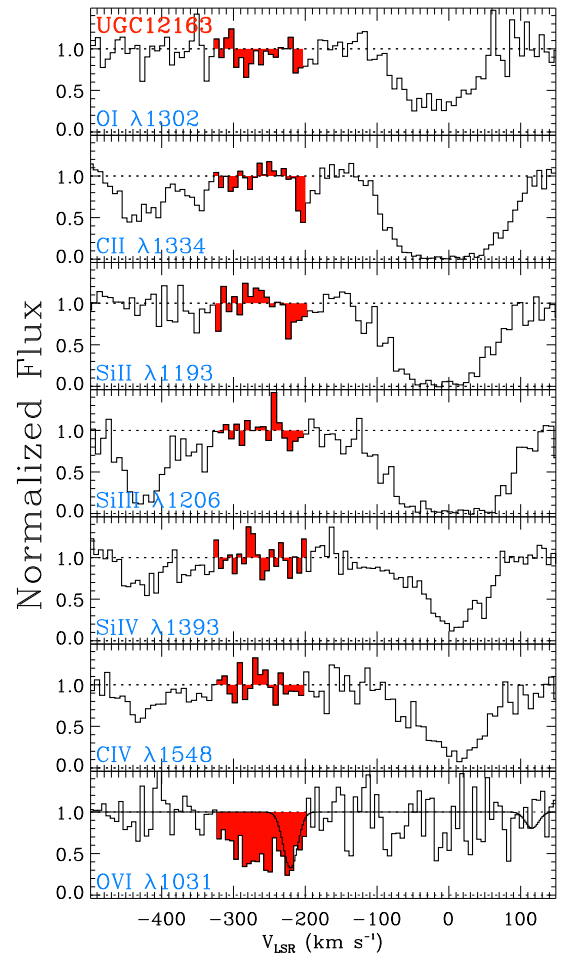


Figure A5. Same as Fig. A1, but for MRK335 at  $R = 287$  kpc.



**Figure A6.** Same as Fig. A1, but for PG0003+158 at  $R = 334$  kpc.



**Figure A7.** Same as Fig. A1, but for UGC12163 at  $R = 339$  kpc.

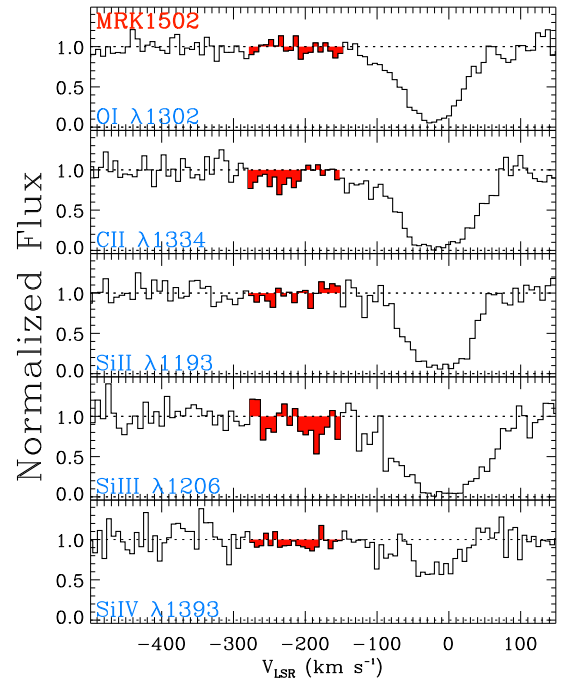


**Figure A8.** Same as Fig. A1, but for MRK1502 at  $R = 361$  kpc.

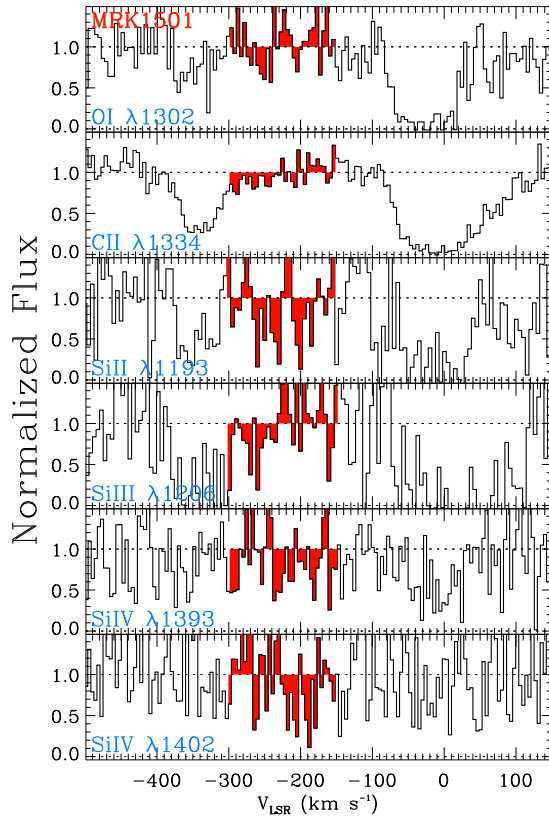


**Figure A9.** Same as Fig. A1, but for MRK1501 at  $R = 389$  kpc.

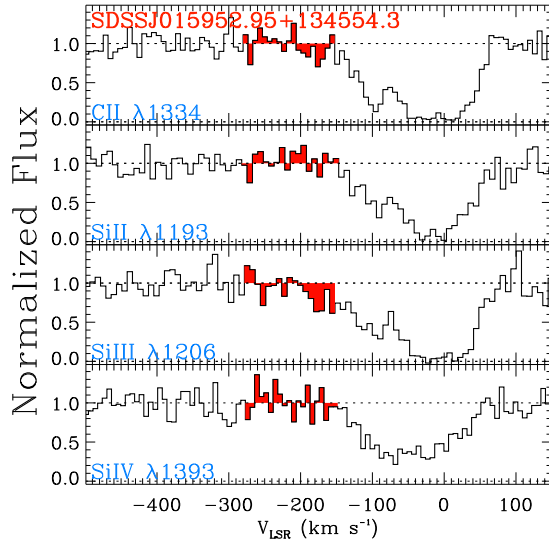


**Figure A10.** Same as Fig. A1, but for SDSSJ015952.95+134554.3 at  $R = 401$  kpc.

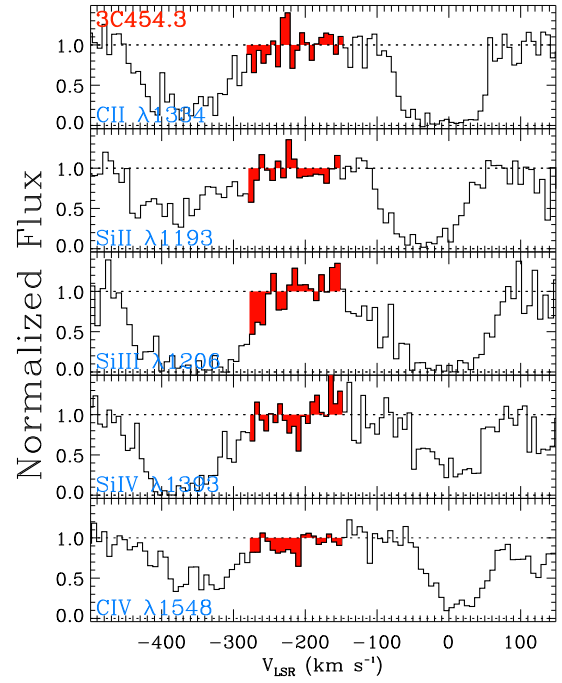


**Figure A11.** Same as Fig. A1, but for 3C454.3 at  $R = 424$  kpc.

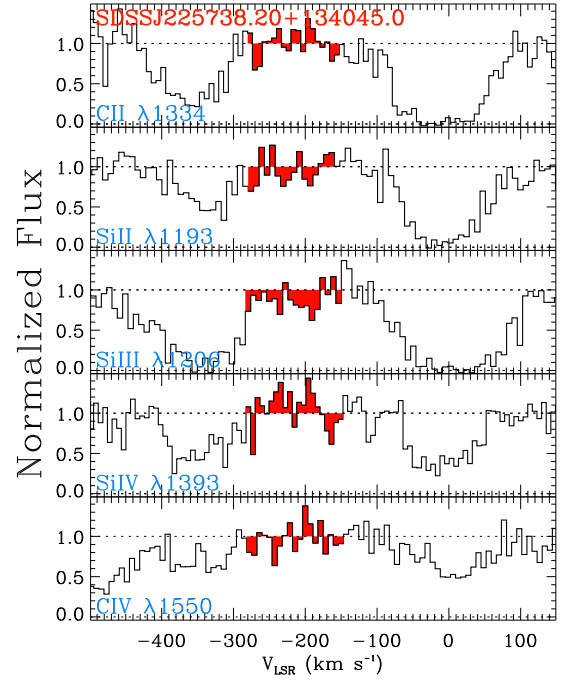


**Figure A12.** Same as Fig. A1, but for SDSSJ225738.20+134045.0 at  $R = 440$  kpc.

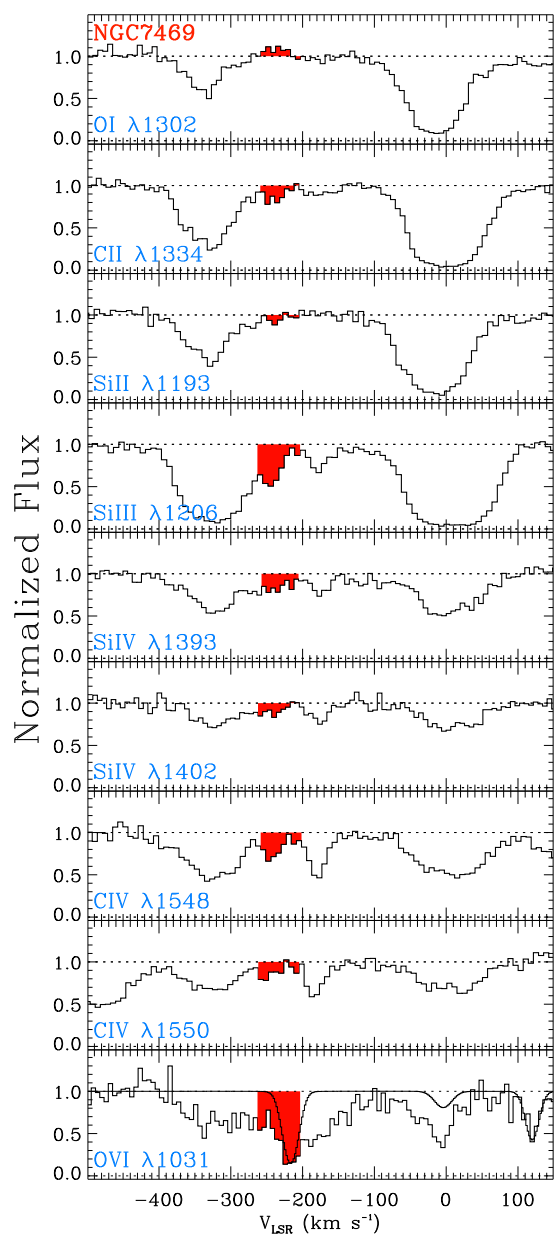


Figure A13. Same as Fig. A1, but for NGC7469 at  $R = 475$  kpc.

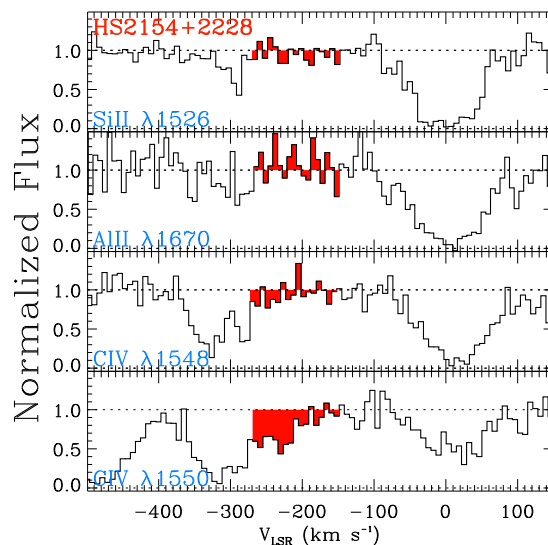


Figure A14. Same as Fig. A1, but for HS2154+2228 at  $R = 476$  kpc.

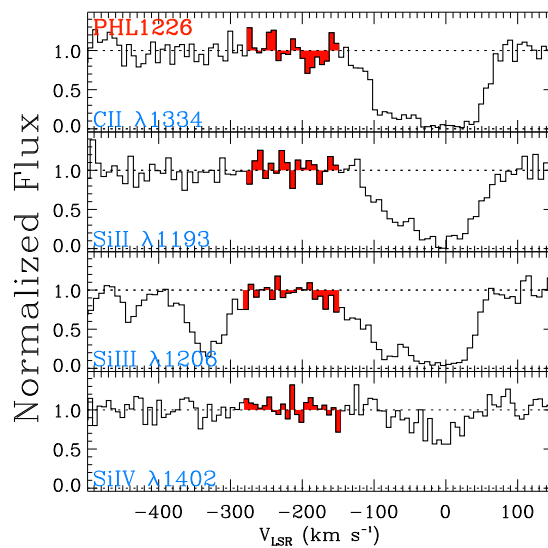
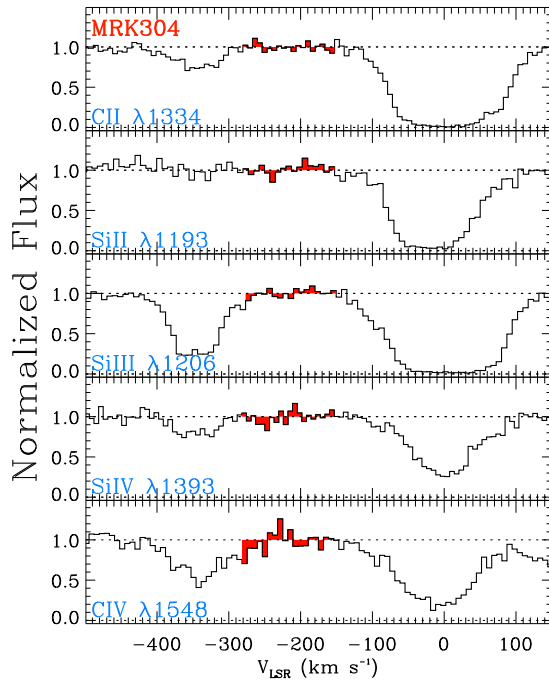
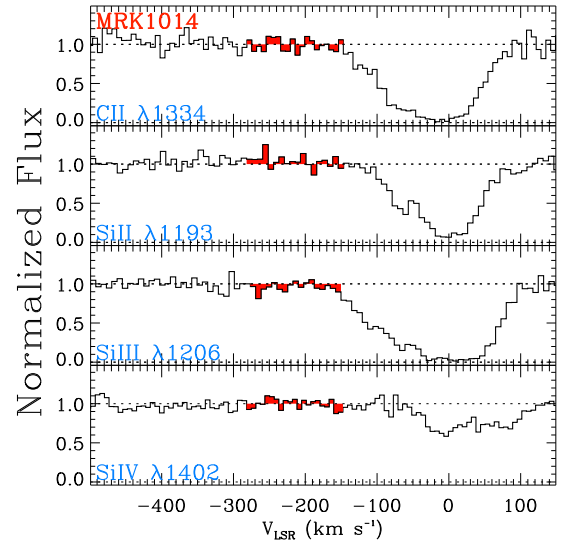


Figure A15. Same as Fig. A1, but for PHL1226 at  $R = 482$  kpc.





**Figure A16.** Same as Fig. A1, but for MRK304 at  $R = 495$  kpc.



**Figure A18.** Same as Fig. A1, but for MRK1014 at  $R = 527$  kpc.

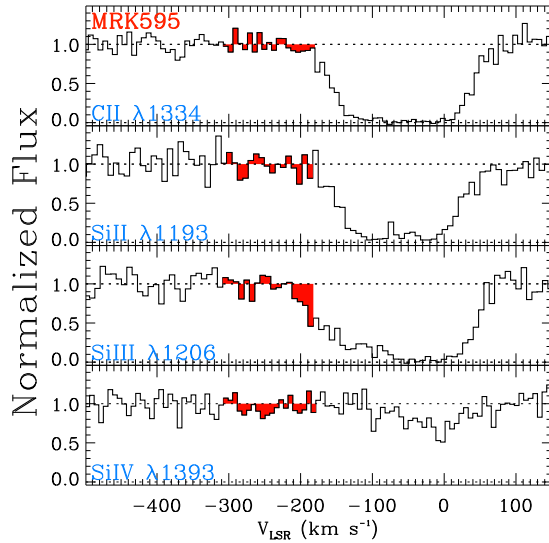


**Figure A17.** Same as Fig. A1, but for MRK595 at  $R = 514$  kpc.